

# Design, simulation and performance of the resistive-anode PICOSEC Micromegas detector

D. Janssens<sup>a</sup>, A. Utrobićic<sup>b,\*</sup>, M. Kovacic<sup>c</sup>, M. Lisowska<sup>a</sup>, R. Aleksan<sup>d</sup>, Y. Angelis<sup>e</sup>, J. Bortfeldt<sup>f</sup>, F. Brunbauer<sup>a</sup>, M. Brunoldi<sup>g,h</sup>, M. Buljan<sup>b</sup>, E. Chatzianagnostou<sup>e</sup>, J. Datta<sup>i</sup>, R. De Oliveira<sup>a</sup>, G. Fanourakis<sup>j</sup>, D. Fiorina<sup>g,h,l</sup>, K. J. Floethner<sup>a</sup>, M. Gallinaro<sup>k</sup>, F. Garcia<sup>l</sup>, I. Giomataris<sup>d</sup>, K. Gnanno<sup>m</sup>, A. Gurpinar<sup>a</sup>, F.J. Iguaz<sup>d,2</sup>, A. Kallitsopoulou<sup>d</sup>, I. Karakoulias<sup>e</sup>, B. Kross<sup>m</sup>, P. Legou<sup>d</sup>, J. Liu<sup>n</sup>, M. Lupberger<sup>o,p</sup>, I. Maniatis<sup>a,e,3</sup>, J. McKisson<sup>m</sup>, Y. Meng<sup>n</sup>, H. Muller<sup>a,p</sup>, E. Oliveri<sup>a</sup>, G. Orlandini<sup>q</sup>, A. Pandey<sup>m</sup>, T. Papaevangelou<sup>d</sup>, M. Pomorski<sup>f</sup>, L. Ropelewski<sup>a</sup>, K. Salamon<sup>b</sup>, D. Sampsonidis<sup>e,s</sup>, L. Scharenberg<sup>a</sup>, T. Schneider<sup>a</sup>, E. Scorsone<sup>d</sup>, L. Sohl<sup>d,4</sup>, Y. Tsipolitis<sup>t</sup>, S.E. Tzamarias<sup>e,s</sup>, I. Vai<sup>g,h</sup>, M. van Stenis<sup>a</sup>, R. Veenhof<sup>a</sup>, P. Vitulo<sup>g,h</sup>, X. Wang<sup>n</sup>, S. White<sup>k</sup>, W. Xi<sup>m</sup>, Z. Zhang<sup>n</sup>, and Y. Zhou<sup>n</sup>

<sup>a</sup>European Organization for Nuclear Research (CERN), CH-1211, Geneva 23, Switzerland

<sup>b</sup>Ruder Bošković Institute, Bijenička cesta 54, 10000 Zagreb, Croatia

<sup>c</sup>University of Zagreb, Faculty of Electrical Engineering and Computing, 10000 Zagreb, Croatia

<sup>d</sup>IRFU, CEA, Université Paris-Saclay, F-91191 Gif-sur-Yvette, France

<sup>e</sup>Department of Physics, Aristotle University of Thessaloniki, University Campus, GR-54124, Thessaloniki, Greece

<sup>f</sup>Department for Medical Physics, Ludwig Maximilian University of Munich, Am Coulombwall 1, 85748 Garching, Germany

<sup>g</sup>Dipartimento di Fisica, Università di Pavia, Via Bassi 6, 27100 Pavia (IT)

<sup>h</sup>INFN Sezione di Pavia, Via Bassi 6, 27100 Pavia (IT)

<sup>i</sup>Stony Brook University, Dept. of Physics and Astronomy, Stony Brook, NY 11794-3800, USA

<sup>j</sup>Institute of Nuclear and Particle Physics, NCSR Demokritos, GR-15341 Agia Paraskevi, Attiki, Greece

<sup>k</sup>Laboratório de Instrumentação e Física Experimental de Partículas, Lisbon, Portugal

<sup>l</sup>Helsinki Institute of Physics, University of Helsinki, FI-00014 Helsinki, Finland

<sup>m</sup>Jefferson Lab, 12000 Jefferson Avenue, Newport News, VA 23606, USA

<sup>n</sup>State Key Laboratory of Particle Detection and Electronics, University of Science and Technology of China, Hefei 230026, China

<sup>o</sup>Helmholtz-Institut für Strahlen- und Kernphysik, University of Bonn, Nußallee 14–16, 53115 Bonn, Germany

<sup>p</sup>Physikalisches Institut, University of Bonn, Nußallee 12, 53115 Bonn, Germany

<sup>q</sup>Friedrich-Alexander-Universität Erlangen-Nürnberg, Schloßplatz 4, 91054 Erlangen, Germany

<sup>r</sup>CEA-LIST, Diamond Sensors Laboratory, CEA Saclay, F-91191 Gif-sur-Yvette, France

<sup>s</sup>Center for Interdisciplinary Research and Innovation (CIRI-AUTH), Thessaloniki 57001, Greece

<sup>t</sup>National Technical University of Athens, Athens, Greece

## Abstract

The PICOSEC Micromegas detector is a Micro-Pattern Gaseous Detector (MPGD) concept developed to achieve tens of picosecond-level timing resolution for charged particle detection by combining a Cherenkov radiator with a two-stage Micromegas amplification structure. To improve operational robustness at high gain and under intense radiation backgrounds, a resistive anode has been implemented using a diamond-like carbon (DLC) layer deposited on a Kapton substrate. While this design enhances detector stability, the resistive layer may influence rate capability, signal formation, and detector capacitance, altering its timing performance.

In this work, a comprehensive study of a resistive PICOSEC design is presented, including an analytical model and finite-element simulation to quantify rate-dependent gain reduction due to ohmic voltage drop in the resistive layer. An analytical solution for the voltage distribution across a finite-size resistive layer is derived, and a numerical model is developed to evaluate gain suppression under intense particle fluxes. For the single-channel prototype geometry and expected beam conditions at the CERN SPS H4 beam line, surface resistivities around  $20\text{ M}\Omega/\square$  are found to ensure discharge protection and acceptable gain stability. The impact of the resistive layer on signal integrity is investigated using an extended Ramo–Shockley formalism with time-dependent weighting fields and Garfield++ simulations. The contribution of delayed signal components induced by the resistive layer is quantified, and a preservation of the leading-edge of the signal was found for surface resistivities exceeding  $100\text{ k}\Omega/\square$ .

Single-channel resistive-anode prototypes were designed ( $\varnothing 10$  and  $\varnothing 15$  mm), constructed, and experimentally characterized. Laboratory measurements using single photoelectrons and a power spectral density analysis show the predicted reduction in signal amplitude due to the insulating layer, while preserving the leading edge of the electron peak. Muon beam tests with both CsI and DLC photocathodes were performed, demonstrating a time resolution of  $11.5 \pm 0.4\text{ ps}$  using CsI, comparable to the  $11.9 \pm 0.4\text{ ps}$  of the metallic-anode device, showing the suitability of the resistive design for precision timing applications in challenging operational conditions.

**Keywords:** Micropattern Gaseous detectors, Micromegas, Cherenkov detectors, Photocathode, Timing detectors, Simulation

## 1. Introduction

The increasing collision densities foreseen in future high-luminosity colliders pose unprecedented challenges for track and vertex reconstruction, with up to about 200 simultaneous proton–proton interactions expected per bunch crossing at the High-Luminosity Large Hadron Collider. Preserving efficient event separation under these pile-up conditions requires detector systems with  $O(10)$  ps timing resolution for minimum ionizing particles, while also tolerating intense particle fluxes and high radiation levels [1]. By incorporating precision timing for track reconstruction, a time-layered approach can be used, which dramatically mitigates pile-up, allowing collisions that overlap in space to be distinguished by their differing time of occurrence. Micro-Pattern Gaseous Detectors (MPGDs) have proven to be robust and scalable [2], offering notable rate capability [3], exhibit good spatial resolution [4], and provide a cost-effective solution for instrumenting large detector areas [5, 6, 7, 8]. However, reaching sub-nanosecond timing precision with gas-based detectors is inherently challenging. The intrinsic timing spread of MPGD signals is limited by the Poissonian fluctuations of the primary cluster position in the gas and the diffusion effects during electron drift. To overcome these limitations, different designs have been proposed to minimize the time jitter [9, 10, 11], yet had difficulty reaching timing precisions of less than  $O(100)$  ps.

The PICOSEC Micromegas (hereafter PICOSEC MM) is a precise timing MPGD developed to achieve a  $O(10)$  ps time resolution for relativistic charged particles. This performance is realized through the implementation of a two-stage Micromegas amplification structure [12], coupled to a Cherenkov radiator that also serves as the detector's entrance window. The radiator, typically a  $\text{MgF}_2$  crystal, is coated with a semi-transparent photocathode such as CsI [13, 14]. A schematic overview of the detector layout and its operating principle is shown in the top panel of Fig. 1. When a relativistic charged particle traverses the Cherenkov radiator, ultraviolet (UV) photons are emitted and subsequently converted into primary photoelectrons by the photocathode over the area covered by the Cherenkov cone. Under a  $\approx 35$  kV/cm electric field, the emitted photoelectrons promptly initiate a Townsend avalanche within the gas volume, reducing the observed time jitter. The amplification process takes place in two distinct regions separated by a woven micro-mesh embedded in the bulk Micromegas [15]: a pre-amplification region of approximately 200  $\mu\text{m}$  above the mesh, and a nominal 128  $\mu\text{m}$  amplification gap mechanically

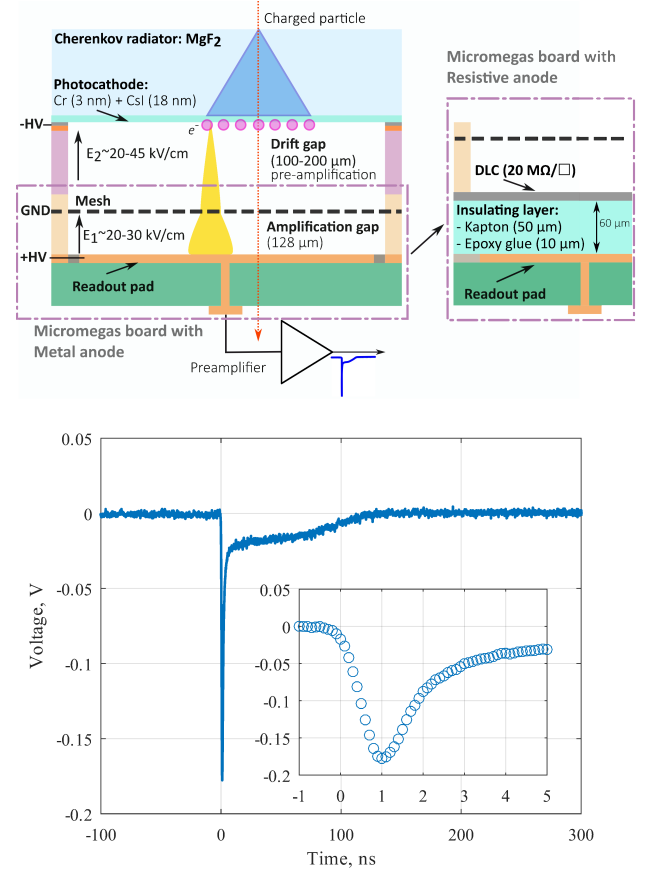


Figure 1: Top: Operating principle of the PICOSEC MM detector. Bottom: Typical PICOSEC MM signal at the output of the amplifier.

defined by pillars between the mesh and the anode plane. The detector operates at atmospheric pressure and room temperature using a gas mixture of 80% Ne, 10%  $\text{CF}_4$ , and 10%  $\text{C}_2\text{H}_6$ , hereafter referred to as the COMPASS gas mixture<sup>5</sup>. Once electrons traverse the mesh, their motion induces a fast current signal on the readout electrodes. A representative waveform is shown in the bottom Fig. 1, where the leading edge of the electron peak constitutes the primary timing observable.

However, operating Micromegas detectors at the high gains of  $O(10^5 - 10^6)$  required for optimal timing performance, or withstanding highly ionizing radiation backgrounds, poses the risk of electrical discharges that can damage the device. To mitigate this, a resistive anode has been introduced in the PICOSEC design. As depicted in the inset of the top Fig. 1, the resistive anode is implemented as a thin diamond-like carbon (DLC) film coated on an insulating Kapton laminate separating the anode from the readout plane. Such a resistive layer offers increased stability: in the event of a spark or excessive current, its high sheet resistance limits the instantaneous current flow,

\*Correspondence to: Ruder Bošković Institute, Bijenička cesta 54, 10000 Zagreb, Croatia

Email address: antonija.utrobicic@irb.hr (A. Utrobicic)

<sup>1</sup>Now at Gran Sasso Science Institute, Viale F. Crispi, 7 67100 L'Aquila, Italy

<sup>2</sup>Now at SOLEIL Synchrotron, L'Orme des Merisiers, Départementale 128, 91190 Saint-Aubin, France.

<sup>3</sup>Now at Department of Particle Physics and Astronomy, Weizmann Institute of Science, Rehovot, 7610001, Israel.

<sup>4</sup>Now at TÜV NORD EnSys GmbH Co. KG.

<sup>5</sup>While being the current baseline mixture it has a relatively high global warming potential of 740 (normalized to  $\text{CO}_2$ ) compared to mixtures such as Ar/ $\text{CO}_2$  (93%/7%) that has 0.07. There is an ongoing effort to look for an alternative gas mixture that can provide a good timing performance [16]

thereby quenching discharges and preventing damage to the detector components. This approach follows the general principle adopted in other resistive MPGDs, e.g., resistive Micromegas [17] and  $\mu$ -Resistive Well ( $\mu$ RWELL) [18] designs, where a surface resistivity of at least  $10 \text{ M}\Omega/\square$  is used to ensure minimal spark protection. However, besides improving the stability against discharges and separating the high voltage from the readout electronics, the resistive anode can adversely impact the detector's rate capability. At very high event rates, the flow of charge in a resistive electrode can produce localized voltage drops (ohmic polarization) that temporarily reduce the effective amplification field. This rate-dependent gain suppression can limit the detector's efficiency and timing performance if the resistivity and grounding scheme are not optimized. Moreover, the presence of a resistive layer influences the signal formation on the readout: the induced current is not only from the movement of the electron-ions pairs in the amplification region but also the reaction of the resistive material due to its finite conductivity. This can result in an alteration of the pulse shape as seen by the front-end electronics by the addition of a delayed signal that, given sufficiently low surface resistivities, can be shared over neighboring readout channels. In addition, the detector capacitance as seen by the electronics is modified, which alters the shaping of the electron peak [19]. Furthermore, the resistive layer acts as a source of Johnson–Nyquist thermal noise [20, 21, 22] in the system, which was treated numerically in Ref. [23]. These signal integrity considerations must be addressed to ensure that the leading edge of the signal pulse is minimally affected, thereby preserving the timing capability of the device.

With the aim of developing a robust multi-channel implementation of the PICOSEC MM detector, a new design based on the resistive readout structure shown in the top Fig. 1 has been developed. In this work, a comprehensive study of the resistive PICOSEC MM design is presented, combining analytical modeling, finite-element simulations, and experimental characterization. The rate capability is estimated through analytical and numerical modeling of the voltage drop in the resistive layer under intense irradiation, allowing the estimation of gain reduction as a function of surface resistivity and particle flux. In parallel, the impact of the resistive layer on signal formation is studied using an extended Ramo-Shockley formalism with time-dependent weighting fields and Garfield++ simulations, quantifying the contribution of delayed signal components and their influence on the leading edge of the electron-peak. Two single-channel resistive-anode prototypes with  $O(10)$  mm active areas were designed, constructed, and characterized. Laboratory measurements using single photoelectrons were performed and compared with their metal-anode counterparts in order to study the predicted signal-amplitude reduction due to the insulating layer and to assess the signal integrity of the electron-peak leading edge. Finally, the timing performance was evaluated in a 150 GeV muon beam at CERN using both CsI and DLC photocathodes, and directly compared with a metallic-anode detector operated under identical conditions.

## 2. Simulations

### 2.1. Rate capability

Because of its non-zero resistance to ground, the resistive anode causes an ohmic reduction of the electric field within the amplification gap when high gains or high event rates are encountered. The decrease in gain that follows adversely affects the gas gain performance, the degree of which is dependent on the surface resistivity  $R [\Omega/\square]$  and precise grounding scheme of the resistive layer. For resistive MPGDs, this *rate effect*, here referring to a device's ability to maintain its gain under a certain event rate per unit area, has been theoretically assessed using various methods. For resistive plane configurations like the one discussed here, previous work estimated the gain reduction as a function of the particle flux  $\Phi [\text{Hz cm}^{-2}]$  for different surface resistivities [24]. This estimation was achieved by taking the limit of the solution to the Telegraph equation [25] in the case of a current being imposed on an infinitely extending resistive layer. While this approach captured the qualitative behavior observed in experimental data, it does not account for the boundaries of the resistive readout. Another approach, focusing on the  $\mu$ RWELL detector, was presented by G. Bencivenni et al. [18]. They provided the average resistance to ground  $\bar{\Omega}$  given the irradiated current over a circular area with a radius  $r_b$  at the center of a circular resistive layer. This resistance could be expressed in terms of the layer's radius  $c$  as  $\bar{\Omega}(c) \simeq R(2c - r_b)/2\pi r_b$ , where the voltage drop can then be calculated using Ohm's first law. A numerical approach was used in another study conducted by Z. Fang et al. [26]. They represented the resistive layer as a discrete electrical system, thus enabling the assessment of the local voltage drops and rate effects for the more complex charge evacuation schemes found in various  $\mu$ RWELL prototypes [27] resulting from a position dependent irradiation current density. This work presents two alternative models, one giving an analytical expression for the potential drop on a finite square resistive layer, and a numerical method based on the Finite Element Method (FEM), where the Maxwell equations are solved under the quasi-static limit. The latter method provides the flexibility to handle systems with greater complexity that are technically more challenging to represent using a circuit-based approach, e.g., vertical charge evacuation through embedded resistors [28, 29], or multiple DLC layers [27, 30, 31].

First, the concept of the voltage drop across a resistive layer under an externally impressed direct current (DC) source will be reviewed, based on which a more complete description of the voltage drop across the finite resistive layer than those discussed above was derived. After this, the gain reduction will be estimated using numerical solutions of the potential in the  $10 \times 10 \text{ cm}^2$  multi-channel design of the resistive anode of Ref. [32] on which a current density from the particle flux is imparted. Using this, the maximum surface resistivity value that allows the resistive PICOSEC design to be effectively operated within a  $\pi$  beam at the H4 Secondary Beam Line facility of the CERN Super Proton Synchrotron (SPS) will be estimated.

### 2.1.1. Voltage drop across a thin resistive layer

In this part, the resistive configuration depicted in the inset of the top Fig. 1 will be examined. This readout structure involves a thin resistive layer electrically connected to the ground and situated along its entire outer boundary at coordinates  $x = 0, a$  and  $y = 0, b$ , which is positioned between the gas gap and the insulating layer. In addition, an amplification field in the gas gap of strength  $E_a$  is applied. Given a charge  $q$  deposited on the resistive layer at  $t = 0$ , currents will start flowing in the resistive layer to compensate for this newly arrived charge, resulting in its seeming decay. As discussed in the work of W. Riegler [33], the dynamics are governed by the infinite number of time constants, the largest of which when  $a = b$  can be approximated to

$$\tau_{11} \approx \frac{1}{2\pi^2} R \left( \varepsilon_1 \frac{a^2}{d} + \varepsilon_2 \frac{a^2}{g} \right) = \frac{1}{2\pi^2} R (C_1 + C_2), \quad (1)$$

with  $C_1$  and  $C_2$  denoting the capacitance from the resistive layer to the readout and mesh, respectively, as if it were treated as a metallic layer. It dictates the time scale over which the charge is horizontally drained by the resistive layer to the ground frame. This happens at a rate set by this maximal time constant of the system, e.g., for  $g = 128 \mu\text{m}$ ,  $d = 60 \mu\text{m}$ ,  $a = b = 10 \text{ cm}$ ,  $\varepsilon_1 = 3.7$ , and  $R = 10 \text{ M}\Omega/\square$  it yields  $\tau_{11} = 3.12 \text{ ms}$ . As indicated by Eq. (1), when the endpoint of the resistive layer is shifted to a greater distance, this time constant increases.

Given several charges deposited in the same region in rapid succession, the combined effects of their electric fields within the amplification gap will lead to a localized reduction in  $E_a$ . In the continues limit, a constant DC-current can be applied to the resistive layer represented as  $q(t) = I_0 t$ , rather than introducing a single charge of  $q(t) = q\Theta(t)$  [34]. The steady-state solution can then be found in the Laplace space through  $\lim_{t \rightarrow \infty} \phi(\mathbf{x}, t) = \lim_{s \rightarrow 0} s\phi(\mathbf{x}, s)$ , resulting in the potential on the resistive layer to be

$$\begin{aligned} \phi_{\text{pt}}(x, y) &= \frac{4I_0 R}{ab} \sum_{l,m=1}^{\infty} \frac{\sin\left(\frac{\pi l x}{a}\right) \sin\left(\frac{\pi l x_0}{a}\right) \sin\left(\frac{\pi m y}{b}\right) \sin\left(\frac{\pi m y_0}{b}\right)}{\pi^2 \left(\frac{l^2}{a^2} + \frac{m^2}{b^2}\right)} \\ &= 2I_0 R \sum_{l=1}^{\infty} \frac{\sinh(l\pi(a - x_>)/b) \sinh(l\pi x_</b)}{\pi l \sinh(l\pi a/b)} \\ &\quad \times \sin\left(\frac{l\pi y_0}{b}\right) \sin\left(\frac{l\pi y}{b}\right), \end{aligned} \quad (2)$$

where the following notation is used

$$x_> := \begin{cases} x_0 & x < x_0 \\ x & x \geq x_0 \end{cases}, \quad x_< := \begin{cases} x & x < x_0 \\ x_0 & x \geq x_0 \end{cases}. \quad (3)$$

In essence, this is the Ohmic relation between the voltage drop, resistance to ground and the injected current. It is worth noting that the dependence on the size and dielectric constants of the gas gap and insulating layer are absent in the steady-state solution, which is fully determined by the electrical properties and dimensions of the resistive layer. Eq. (2) can be used to deter-

mine the potential drop over the resistive layer away from the beam spot. However, given the point-like injection of a current  $I_0 \delta(x - x_0) \delta(y - y_0)$  the solution diverges for  $(x, y) \rightarrow (x_0, y_0)$ . To account for a spatially extending beam profile, a uniform distribution of the events across a circular disk with radius  $r_b$  is assumed. When centering the disk at a position  $(x_c, y_c)$ , the voltage drop across the resistive layer is given by

$$\begin{aligned} \phi_{\text{disk}}(x, y) &= \frac{8RI}{abr_b} \sum_{l,m=1}^{\infty} \frac{J_1(r_b k_{lm})}{k_{lm}^3} \sin\left(\frac{\pi l x}{a}\right) \sin\left(\frac{\pi m y}{b}\right) \\ &\quad \times \sin\left(\frac{\pi l x_c}{a}\right) \sin\left(\frac{\pi m y_c}{b}\right), \end{aligned} \quad (4)$$

where  $I$  denotes the total current over the disk,  $J_n(x)$  the  $n$ 'th order Bessel function of the first kind, and

$$k_{lm} := \pi \sqrt{\frac{l^2}{a^2} + \frac{m^2}{b^2}}. \quad (5)$$

To evaluate Eq. (4) numerically, an error term can be defined that quantifies the loss incurred by truncating the summation at maximum values  $l \leq L_{\text{max}}$  and  $m \leq M_{\text{max}}$ , thereby neglecting the tail of the summation. Writing the error as  $\epsilon = \|\text{tail}\|_{\infty}$ , the evaluation can be performed up to

$$L_{\text{max}} \approx \frac{a\kappa}{\pi} \quad \text{and} \quad M_{\text{max}} \approx \frac{b\kappa}{\pi}, \quad (6)$$

with

$$\kappa = \left[ \frac{32\sqrt{2}}{3\pi^{7/2}} \frac{RI}{r_b^{3/2}\varepsilon} \right]^{2/3}. \quad (7)$$

Taking  $\epsilon = 10 \text{ mV}$  for a  $10 \times 10 \text{ cm}^2$  resistive layer of  $10 \text{ M}\Omega/\square$  on which a constant current of  $1 \mu\text{A}$  is impressed uniformly on disk of radius  $7.5 \text{ mm}$ , the sum can be truncated to  $L_{\text{max}} = M_{\text{max}} \approx 180$ .

An example is presented in Fig. 2 for a  $10 \times 10 \text{ cm}^2$  resistive layer irradiated with two different sized beam spots. Given a central position of the beam spot, the voltage drop caused by the constant current deposition on the resistive readout structure is at its highest at the center of the beam profile on the active area. Subsequently, it gradually tapers as it extends towards the periphery of the beam spot, and its impacts can be detected throughout the entire resistive layer. If the total current  $I$  is kept constant, the potential drops towards the Dirichlet walls is identical outside disks of different radii. However, the potential inside the disk tend to drop for larger  $r_b$  as the current is divided over a larger areas. Furthermore, as the current is more efficiently drained the closer it is impressed to the edges of the resistive layer, the maximum voltage drop is not necessarily at the center of the disk when shifting the disk towards edge of the border, breaking the symmetry of the system. Using Eq. (4), the average potential across the disk is then given

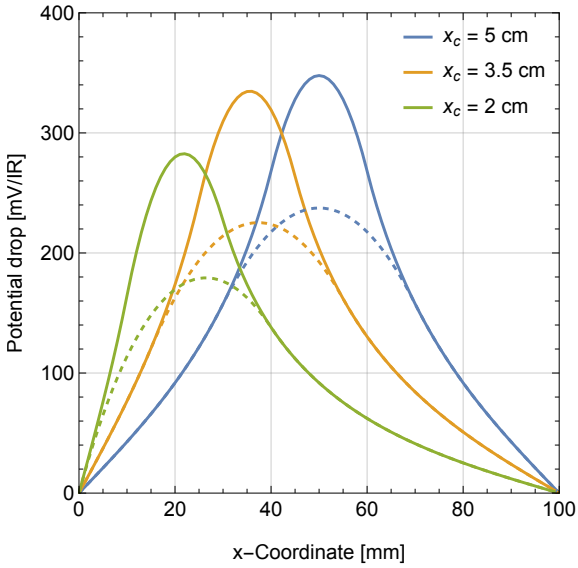


Figure 2: Cross-section at  $y = 50$  mm of the potential drop across a  $10 \times 10$   $\text{cm}^2$  grounded resistive layer with surface resistivity  $R$  with an impressed total current  $I$  across a disk centered at  $(x_c, y_c = 5 \text{ cm})$  with radius  $r = 1 \text{ cm}$  (full lines) and  $r = 2 \text{ cm}$  (dashed lines).

by

$$\bar{\phi}_{\text{disk}}(x_c, y_c) = \frac{16RI}{ab^2} \sum_{l,m=1}^{\infty} \frac{J_1^2(r_b k_{lm})}{k_{lm}^4} \sin^2\left(\frac{\pi l x_c}{a}\right) \sin^2\left(\frac{\pi m y_c}{b}\right), \quad (8)$$

which is dependent on the location of the beam spot on the resistive layer and the constant current  $I$ . As will be explored in the next sub-section, when the potential on the resistive layer changes, the gain will be affected, modifying the value of  $I(\bar{\phi}_{\text{disk}}) \propto \exp(c_1 \bar{\phi}_{\text{disk}})$ , with proportionality constant  $c_1$ . This in turn, introduces a feedback process, that will influence  $\bar{\phi}_{\text{disk}}$ . As a result, the equilibrium value of  $\bar{\phi}_{\text{disk}}$  of Eq. (8) can be expressed in terms of a Lambert W function [35].

### 2.1.2. Estimating gain reduction at high particle fluxes

Due to spatial constraints on the Printed Circuit Board (PCB), the final design of the resistive anode layer uses eight termination points as shown in Fig. 3, instead of connecting it along its entire outer edge as was the premise before. A  $10 \text{ M}\Omega$  resistor is connected to each of these points to ensure the minimal impedance at every point on the active area to avoid destructive capabilities of the discharges resulting in the damaging of the DLC layer. These additions require the use of a FEM approach to determine the steady-state solution of the voltage drop across the resistive layer given a circular  $\pi$  beam profile with a rate of 1.9 MHz. For the exponential relation between the amplification gain and the voltage difference of the mesh and anode, the resulting decrease in gain can be estimated.

Given the  $10 \times 10 \text{ cm}^2$  geometry shown in Fig. (3), a constant boundary DC-current source  $\mathbf{j}_e(x, y, t)$  is impressed on the resistive layer starting at  $t = 0$ . As an ansatz, the beam spot

is taken to be circular with a radius of  $r_b$  centered in the active area. In polar coordinates, the externally applied current density can be expressed in terms of the particle flux per surface area  $\Phi$  as

$$\mathbf{j}_e(r, t) = -e_0 n_p G_e \Phi \Theta(r_b - r - a) \Theta(t) \hat{\mathbf{z}}, \quad (9)$$

where  $e_0$  denotes the electron charge, and  $G_e$  is the effective detector gain given an applied voltage  $V_a$  on the anode. The number of primary charges  $n_p$  depends on the quantum efficiency of the photocathode used, and for what follows will be taken as  $n_p = 5$ , which is a conservative overestimation for a DLC photocathode [14]. In addition, the beam's radius is fixed to  $r_b = 7.5 \text{ mm}$ . Solving Maxwell's field equations using the electrical currents module within the COMSOL® toolkit [36], the steady-state solution was obtained for various values of  $G_e$ ,  $\Phi$ , and  $R$ . An example of the potential value across the resistive layer is shown in Fig. 3. Unlike Fig. 2, the potential does not reach zero at the connection points of the resistive layer due to the presence of the termination resistors. Following Ohm's law, this sets a lower bound to the rate capabilities even if  $R \rightarrow 0$ , since a global voltage drop will occur over the entire layer due to the constant current flowing through the  $1.25 \text{ M}\Omega$  equivalent resistor. What is more, due to the symmetry of the system, the current is equally drained over all connection points, while shifting the position of the beam towards the corners of the active area, an increase in the voltage drop was found proportional to the increased current that flowing over the two neighboring resistors.

Given an amplification field resulting from the potential difference  $V_a$  between the grounded mesh and the anode plane, an additional average voltage drop in the beam spot  $\bar{\phi} := \int_A \phi(x, y) dA / \pi r_b^2$  can be added. The result in the irradiated circular area for fixed  $\Phi$ , and  $V_a$  is shown in Fig. 4, where  $G_e$  is plotted as a function of the average voltage in the beam spot  $V_a + \bar{\phi}$  that it causes. Until now, the value  $G_e$  was taken to be independent of the local alteration of the anode voltage due to the charge deposition on the resistive layer, while in actuality, it will be coupled

$$G = \exp[c_1(V_a + \bar{\phi}) + c_2], \quad (10)$$

where the parameters  $c_1$  and  $c_2$  depend on the gas properties and detector field configuration. As sufficient time passes, an equilibrium state  $G$  is established where the surface current density impressed on the resistive layer leads to a voltage reduction in the irradiated area, ultimately resulting in an effective gain that matches the generated surface current density as given by Eq. (9). To find this stable point, the free parameters in the above relation between the effective gain  $G_0$  and  $V_a$ , i.e., the *gain curve* of the detector, must be first be estimated in the absence of any rate effects.

The gain curve of the amplification region for the detector can be either obtained through simulation or experiment by varying the amplification field and counting the arrived

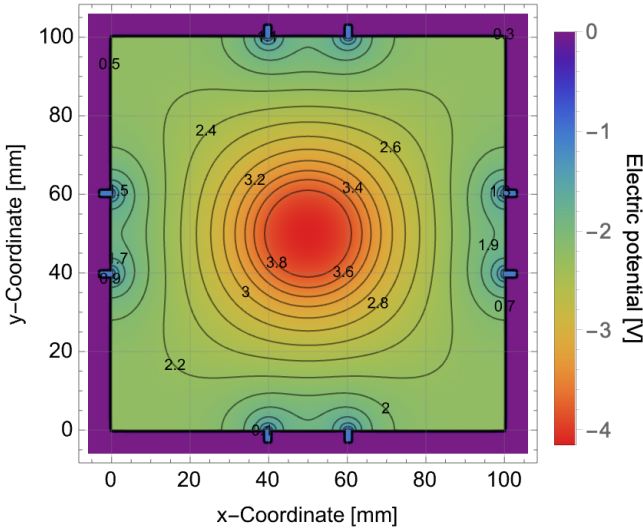


Figure 3: Electric potential  $\phi(x, y)$  across the resistive layer due to the injection of a current density coming from a 15 mm wide circular beam with a flux of  $\Phi = 5.66 \cdot 10^5 \text{ cm}^{-2}\text{s}^{-1}$  and effective detector gain  $G_e = 10^6$ .

charge per event. Going with the experimental approach, a resistive single-channel prototype was used, featuring a pre-amplification gap size of 200  $\mu\text{m}$ . The current  $I_a$  on the anode plane resulting from a uniform and  $O(1)$  kHz low-intensity UV LED irradiation was measured using a pico-ampere meter. Knowing the single photoelectron event rate  $f_{pe}$  through the areas of the pulse height spectra for a fixed exposure time using a digital multichannel analyzer (MCA)<sup>6</sup>, the gain could be estimated using  $G_0 = f_{pe}/e_0 I_a$  for different (pre-)amplification fields. The results for two different cathode voltages are plotted in Fig. 4 alongside the fitted curves of Eq. (10) to estimate the trends. Here, the anticipated exponential relationship can be observed, where the fit adequately describes the data.

Following Eq. (9) when  $G_e = G_0$ ,  $j_e$  constitutes the expected current density after irradiating over a long time scale, i.e., when the system is in equilibrium. Consequently, the steady-state solution for voltage drop and gain can be estimated by identifying the point of intersection between the two curves. In Fig. 5 the gain drop curve is shown as a function of the anode voltage given a 1.9 MHz event rate. For operational voltages of  $V_c = -475 \text{ V}$  and  $V_a = 275 \text{ V}$  the expected gain is reduced by 5.24% and 8.87% for  $R = 10 \text{ M}\Omega/\square$  and  $R = 20 \text{ M}\Omega/\square$ , respectively. While in this model, an ideal beam of pions is considered, in actuality, there will be contamination with particle showers from the interaction of the meson with the material of the experimental setup. This results in a significant increased energy deposit inside the detector geometry, yielding a temporary higher current density on the resistive layer, the degree of which is a function of the rate at which these showers occur. Hence, the results presented here can be regarded as the most

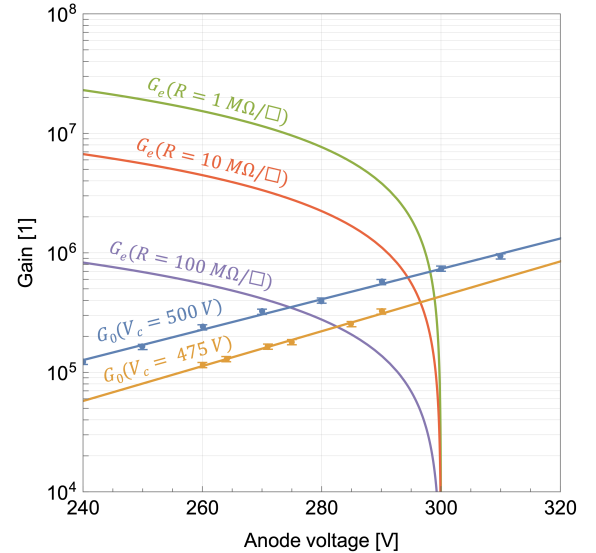


Figure 4: Computed relation between the gain  $G_e$  of the externally applied current density  $j_e$  on the resistive layer as a function of the average voltage drop  $V_a + \bar{\phi}$  on the anode. Furthermore, the measured gain is depicted, represented as  $G_0$ , for diverse (pre-)amplifications, indicating the data points with markers, where a 5% error is assumed. The full lines signify the exponential fits for the two gain curves, employing Eq. (10). The equilibrium state can be identified as the point of intersection between  $G_0$  and  $G_e$ .

favorable scenario.

### 2.1.3. Choice of surface resistivity

The steady-state solution of the local anode potential for different surface resistivities was obtained by combining the FEM numerical results of the simulated potential drop on the anode layer and the measured gain curve using low rate single photoelectron events. Considering the spatial variation of the voltage drop, denoted as  $\phi(x, y)$ , across the readout plane, implementing gain compensation via an increase in the applied anode voltage will uniformly elevate the amplification field. This elevation can lead to undesirably high gains in regions beyond the beam profile. Furthermore, in cases of non-constant event rates at intermittent intervals without incoming particles, the system will relax to its initial state, leading to an amplification field that surpasses the desired level. Notably, a below 20% gain drop is found for a surface resistivity of  $20 \text{ M}\Omega/\square$ .

Depending on the final HEP application requirements, this calculation can be repeated with the beam-relevant parameters. This outcome was taken into account, along with the minimal discharge protection prerequisites and a negligible reduction to the rising edge of the electron peak due to the delayed component of the signal (as discussed later), and the final surface resistivity value for production was fixed at  $20 \text{ M}\Omega/\square$ .

This simple resistive layout only allows the evacuation of the deposited charge along the edges of the geometry. Therefore, this design is not scalable for high-rate applications requiring extensive surface area coverage. Within the development of resistive layer-based readout structures within the MPGD fam-

<sup>6</sup>Amptek MCA-8000D, <https://www.amptek.com/products/multichannel-analyzers/mca-8000d-digital-multichannel-analyzer>.

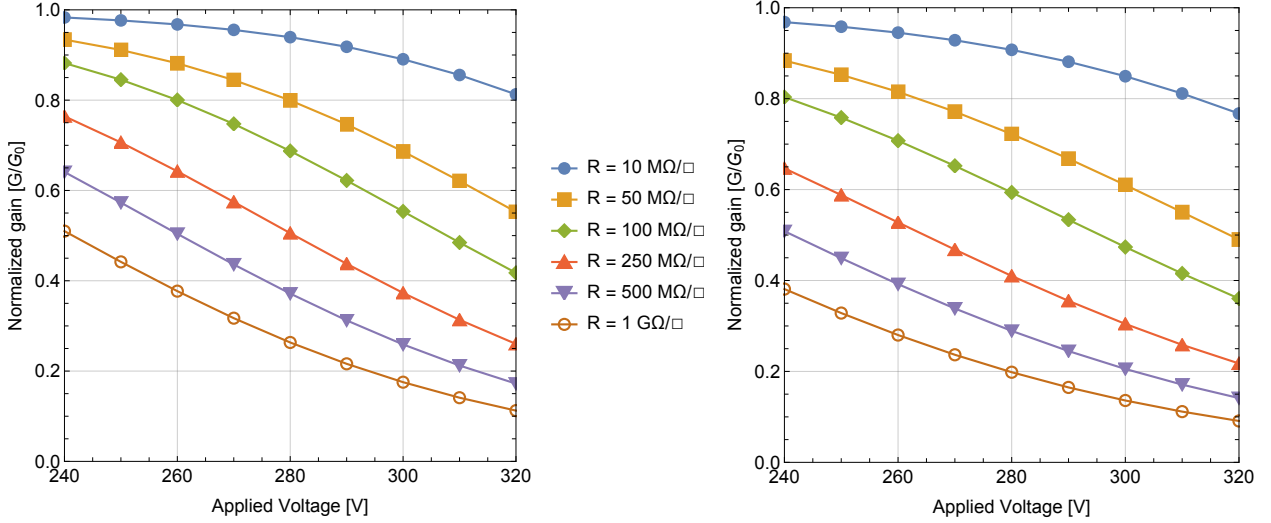


Figure 5: Calculated normalized gain for the resistive PICOSEC as a function of the applied anode voltage  $V_a$  for different surface resistivities and cathode voltage of  $-475$  V (left panel) and  $-500$  V (right panel).

ily, more sophisticated ‘local’ charge evacuation schemes have been devised that are suitable for large area coverage [27]. One such structure is realized through the implementation of draining vias in a double resistive layer layout, with the bottom layer ensuring minimal protective impedance [28, 29, 27, 30, 31]. These types of rapid grounding techniques hold the potential to overcome the typical rate limitations associated with large-area resistive readout structures and are now being studied for the multi-channel resistive PICOSEC designs [37].

## 2.2. Signal integrity

Incorporating a resistive layer into the readout structure of the robust PICOSEC MM design introduces an impact on the overall signal shape coming from the resistive layer’s finite conductivity and the insulating laminate’s presence. Crucial for timing measurements, this influence can adversely affect both the shape and amplitude of the leading-edge of the signal induced on the pad electrodes. The subject of the ‘transparency’ of the resistive layer to a signal generated by charges moving above it and the induction on the readout electrodes located below has been a longstanding topic in detector R&D [38]. A classic example is the contribution to the timing performance from the graphite layers, which form an integral part of contemporary (M)RPCs designed for the HV application and avalanche charge dissipation. Due to the finite conductivity of these layers, the reaction of this resistive element will result in the emergence of a delayed component to the signal, which negatively contributes to the signal amplitude due to its opposite polarity to the prompt current. It is now well understood that this contribution is negligible for the typical value of  $O(300)$   $\text{k}\Omega/\square$  of this material. A seminal study on this topic was performed by G. Battistoni et al. in 1982 [38] who utilized a lumped element equivalent circuit to estimate the signal transparency of a thin resistive cathode layer, which divides the gas volume of a MWPC from an insulating layer containing AC-coupled

closely spaced strip electrodes. As described in Ref. [33], this approach hinges on the ability to define a capacitances between the resistive layer and electrodes, which only holds at late times. Instead, to be compatible with the quasi-static Maxwell equations, an extension to the the Ramo-Shockley theorem [39, 40] can be used to estimate the contribution from the resistive material to the induction of the electron peak found in the resistive PICOSEC design.

### 2.2.1. Time-dependent weighting potentials

The induction of signal on electrodes in the presence of resistive materials can be described by using an extended form of the Ramo-Shockley theorem for conductive media. The contribution of the material resistivity to the signal formation is included in the time evolution of the weighting potential, which is the solution of the Maxwell equations in the quasi-static limit [41, 42, 43, 44]. Consider a resistive detector with  $N$  electrodes indexed  $i \in \{1, 2, \dots, N-1, N\}$  and a point charge carrier  $q$  that follows a path  $\mathbf{x}_q$  parametrized by time  $t$ . The induced signal on the electrodes is then given by

$$I_i(t) = -\frac{q}{V_w} \int_0^t dt' \mathbf{H}_i [\mathbf{x}_q(t'), t-t'] \cdot \dot{\mathbf{x}}_q(t') , \quad (11)$$

where the dot notation refers to the derivative with respect to time and the weighting vector of electrode  $i$  is a function of its dynamic weighting potential  $\Psi_i$  through

$$\mathbf{H}_i(\mathbf{x}, t) := -\nabla \frac{\partial \Psi_i(\mathbf{x}, t) \Theta(t)}{\partial t} . \quad (12)$$

Here, the time-dependent weighting potential is obtained by removing the drifting charge carriers and applying the boundary conditions

$$\Psi_i(\mathbf{x}, t)|_{\mathbf{x} \in S_j} = \delta_{i,j} V_w \Theta(t) , \quad (13)$$

with  $S_j$  denoting the surface of electrode indexed  $j$ ,  $\delta_{i,j}$  the Kronecker delta function and  $\Theta(t)$  the Heaviside distribution. The contribution from the direct induction of signal sourced by the movement of the charge carrier (called the *prompt component*), and the part coming from the response of the resistive materials (*delayed component*) can be disentangled on the weighting potential level by  $\Psi_i(\mathbf{x}, t) := \psi_i^p(\mathbf{x}) + \psi_i^d(\mathbf{x}, t)$ , with the delayed weighting potential being defined as  $\psi_i^d(\mathbf{x}, 0) = 0$ .

In what follows the resistive geometry depicted in the top Fig. 1 will be used, where a thin resistive layer with a surface resistivity  $R$  positioned between the amplification gap of size  $g$  and the insulating layer with thickness  $d$  is terminated around its entire outer edge situated at  $x = 0, 10$  cm and  $y = 0, 10$  cm. Since the main focus is in the formation of the signal on the  $1\text{ cm}^2$  square pad electrodes on the readout plane, only the movement of the charges below the micro-mesh will contribute to this. Therefore, the amplification gap structure in the top Fig. 1 is approximated as a parallel plate geometry. While the analytical solution can be obtained using Ref. [33], the evaluation of the non-closed solution converges slowly for the dimensions of the Micromegas. Instead, it was chosen to use the more computationally efficient numerical FEM recipe found in [45, 46]. Given a Townsend avalanche that occurs in the amplification region, the contribution of the delayed component to the electron peak was assessed as a function of the parameter  $R$  and the relative position of the avalanche with respect to the pad electrode. The dynamic weighting potential was calculated for the central pad, i.e.,  $x_p = y_p = 5$  cm, for different surface resistivities and subsequently integrated into a Monte Carlo model for the avalanche development.

### 2.2.2. Charge carrier simulation

In order to calculate the expected change of the leading-edge of the signal induced on the  $1 \times 1\text{ cm}^2$  readout pads with the introduction of the resistive layout, the above formalism is used in the open-source Monte Carlo simulation toolkit Garfield++ [47]. With the dynamic weighting potential being obtained numerically, it can be convoluted with the simulated drift lines of the electron and ions inside the gas [48].

For the propagation of these charge carriers through the gas, the applied electric field configuration needs to be defined. Similarly to the approach used to obtain the dynamic weighting potential, a FEM approach is used to solve the Laplace equation. Using unit cell  $a$  of the geometry, mirror periodicity is used on the xz- and yz-boundaries, while Dirichlet boundary conditions are imposed for the cathode (-455 V), micro-mesh (0 V), and anode (275 V). Having the electric field map, the COMPASS gas mixture with a Penning transfer rate of  $r_p = 0.5$  [49] is used to microscopically simulate the movement of the electrons and the formation of a Townsend avalanche starting from a single photoelectron [50]. For the ions, measured reduced mobilities of  $\text{Ne}^+$  in pure Ne [51, 52] were used to perform a Monte Carlo integration of their drift paths, neglecting any possible ion chemistry inside the gas [53, 54]. As the electrons traverse the micro-mesh into the amplification region, the signal induc-

tion process on the readout pads starts. The resulting induced current can be treated as an ideal current source in an LTSpice model [55] that incorporates of the pad capacitance along with the current amplifier's response.

### 2.2.3. Electron-peak amplitude

An example prompt signal  $I^p$  and delayed signal  $I^d$  from a Townsend avalanche is shown in Fig. 6 (top) for three different surface resistivities. Although the ion tail is indeed accounted for, its amplitude is significantly smaller in comparison to the electron signal, causing the ion tail to be nearly imperceptible due to the fine signal binning. The amplitude of the prompt component resulting from the instantaneous induction of signal from the movement of both the electrons and ions below the mesh is subject to the relative permittivity  $\varepsilon_r$  and thickness of the insulating layer. Compared to the non-resistive design where this laminate is absent, this results in a fundamental signal reduction by a factor  $f_p$ , which in the limit of  $w_x \gg g$  can be written as

$$f_p := \frac{E^p(d)}{E^p(0)} = 1 - \frac{d}{d + \varepsilon_r g}, \quad (14)$$

where the prompt weighting field of a readout plane bellow an insulating layer was used

$$\mathbf{E}^p(d) = \frac{\varepsilon_r V_w}{d + \varepsilon_r g} \hat{\mathbf{z}} \quad (15)$$

with the relative permittivity  $\varepsilon_r$ , the thickness of the insulating layer  $d$ , and the size of the amplification gap  $g$ . In the case of the resistive PICOSEC MM, this corresponds to a value of  $f_p = 0.89$ . The response of the resistive layer, as captured by the delayed component of the signal, occurs over a longer time as  $R$  grows, such that for large surface resistivities this contribution can be neglected inside the initial  $\approx 1$  ns time range of the electron peak.

As an indicator for the contribution of the resistive layer to the electron peak amplitude, the *relative peak amplitude* is defined as the ratio between the prompt signal and the total signal:  $\text{Min}[I^p(t) + I^d(t)] / \text{Min}[I^p(t)]$ . This is plotted as a function of different surface resistivities in Fig. 6 (bottom). A heightened sensitivity to the resistive layer's behavior can be observed at the periphery of the pad electrode due to the more immediate signal spreads over the adjacent channels. As  $R \gtrsim 100\text{ k}\Omega/\square$ , a regime is entered in which the electron peak of the induced signal is virtually unaffected by the delayed component of the signal. This outcome remains consistent even when accounting for the response of the pulse amplifier that reads out the channels. This was accomplished by utilizing an LTSpice amplifier model, treating the induced signals as ideal current sources.

In conclusion, due to the occurrence of avalanches in the amplification region over the several mm wide area covered by the radiator's Cherenkov cone, coupled with the lack of prior knowledge regarding the particle's hit position, it is impera-

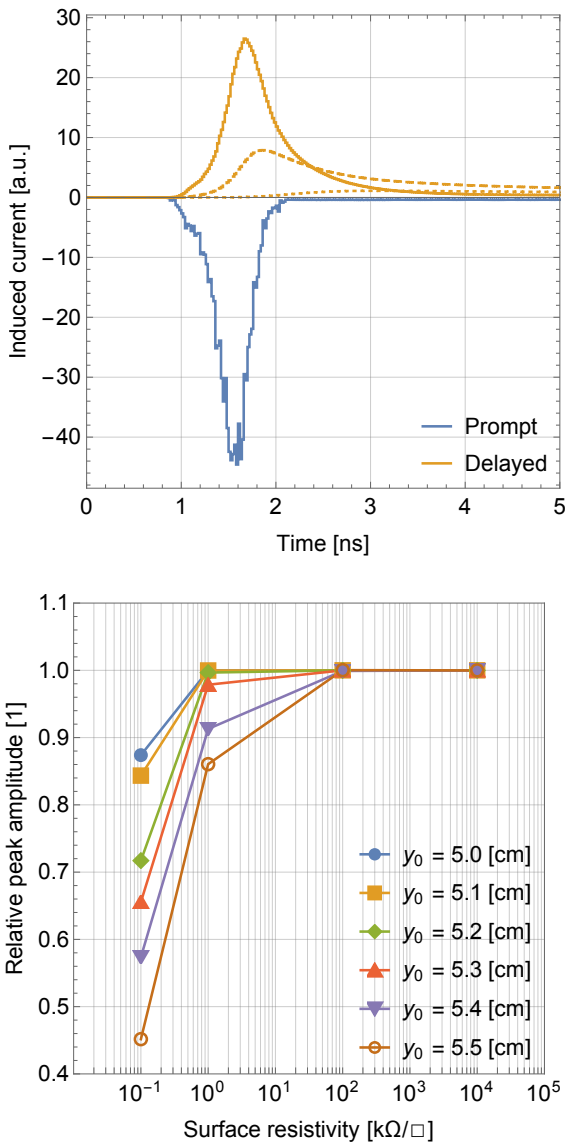


Figure 6: Top: The prompt and delayed components of the induced signal on the 1 cm wide square pad, which is positioned at the center of the active area ( $x_p = y_p = 5$  cm), are determined for a Townsend avalanche initiated at the top of the amplification gap, specifically at the point centered at  $x_0 = 0$  and  $y_0 = 5.4$  cm. The result is given for  $R = 100 \Omega/\square$  (full line),  $R = 1 k\Omega/\square$  (dashed line), and  $R = 100 k\Omega/\square$  (dotted line). Bottom: The relative peak amplitude as a function of the surface resistivity for different avalanche positions on the pad where  $x_0 = 0$ . The plot markers represent the calculated values, while the lines are to guide the eye.

tive to reduce the impact of the DLC layer's response on the leading-edge of the signal across the entire surface of the readout pad. It was found that for surface resistivities exceeding  $100 k\Omega/\square$ , the electron peak is unaffected by the delayed component on the signal. However, an overall amplitude reduction of around 11% must be contended with due to the presence of the  $60 \mu\text{m}$  thick insulating layer between the amplification gap and the readout plane. This model can be further developed in order to describe the relation between the temporal resolution for the case of surface resistivities below  $100 k\Omega/\square$ . Furthermore, it

has the potential to quantify the extent of enhancement in spatial resolution attributable to signal propagation to neighboring channels by including the weighting potentials of the adjacent pads in the calculation.

### 3. Single channel resistive PICOSEC MM design

The single-channel resistive-anode PICOSEC MM detector is based on the metal-anode design reported in [19], modified to incorporate a resistive readout structure. The mechanical layout and internal detector components, including the chamber body, PEEK insert, drift-gap spacers, and  $\text{MgF}_2$  Cherenkov radiator with deposited photocathode, were kept identical in order to isolate the impact of the resistive anode on detector performance. Only the Micromegas and outer readout boards were redesigned to accommodate the resistive layer and its biasing scheme.

The Micromegas board was manufactured from a double-layer FR4 substrate with a total thickness of 3.2 mm. The top and bottom layouts of the resistive board are shown in Fig. 7. The top side, shown in upper right Fig. 7, consists of a circular copper readout pad ( $\varnothing 10$  mm or  $\varnothing 15$  mm), surrounded by a grounded copper ring of 5 mm width, and an additional outer copper ring for the application of the positive high-voltage (HV) bias to the resistive layer. A  $50 \mu\text{m}$  thick Kapton foil carrying a patterned DLC resistive coating is glued with  $10 \mu\text{m}$  epoxy glue on top of the MM board, as shown in upper right and bottom left Figs. 7. The resistive layer consists of a central active disk matching the readout pad diameter, along with three  $\approx 9$  mm extensions reaching toward the edge of the MM PCB for +HV biasing. The layout on the bottom side features a central pad for signal readout, three wider pads for the GND connection, and three shorter pads for the +HV connection, as illustrated in bottom right Fig. 7.

The stainless steel micro-mesh, with a pitch of  $45 \mu\text{m}$  and wire diameter of  $18 \mu\text{m}$ , is embedded on top of the MM board between two insulating layers as shown in Fig. 8 (left). Three pockets in both the top and bottom insulating layers provide the GND electrical contact to the mesh, while three additional apertures allow for gas circulation through the amplification region. As shown in the inset of the top Fig. 1, the thickness of the bottom insulating layer (nominally  $\approx 128 \mu\text{m}$ ) mechanically defines the amplification gap. The detector assembly is done in the same way as described in Ref. [19], in which a spacer is placed above the top insulating layer to define the drift gap thickness and to provide the -HV electrical connection to the photocathode deposited on the bottom side of the  $\text{MgF}_2$  crystal, as depicted in Fig. 8 (middle). The spring-loaded pin system used for HV biasing and GND is shown in Fig. 8 (left), ensures the electrical contact between the detector electrodes and the external circuitry. Compared with the metal anode detector, the resistive design has six ground connections instead of nine and distributes the resistive anode HV bias over three remaining contact points, each routed through

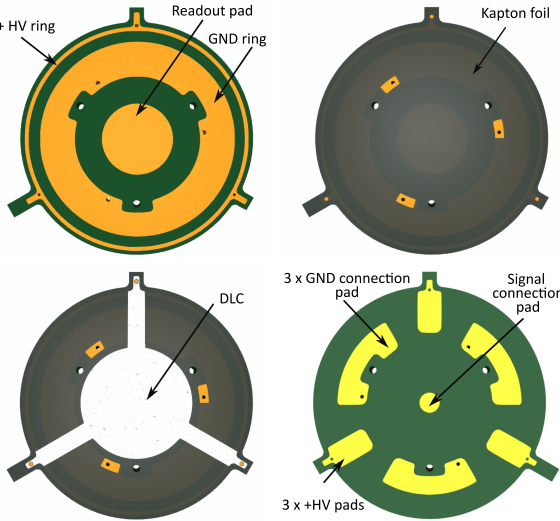


Figure 7: Resistive Micromegas board top (upper left, upper right, and lower left) and bottom side layout (lower right). Upper left: Top copper layer that includes a central readout pad surrounded by the GND plane and a thin HV ring at the outer board perimeter. Upper right: Kapton foil covering the top copper surface. It includes three square openings that enable mesh connections to the GND, three holes to allow gas circulation, and three circular openings at the outer board edge for +HV connection. Bottom left: Circular DLC layer with three extensions toward the board edge for HV connection. Bottom right: Bottom copper layer that has a central signal connection pad, three GND connection pads and three HV connection pads.

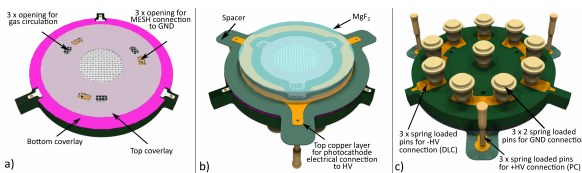


Figure 8: Left: 3D model of a top side Resistive Micromegas board showing mesh integrated between the insulating layers. Middle: 3D model of Resistive MM board, spacer and  $\text{MgF}_2$  crystal arrangement within the detector. Right: 3D model of spring-loaded pins arrangement for electrical connection of the mesh to the GND, photocathode to the -HV and DLC layer to the +HV.

an external  $10 \text{ M}\Omega$  quenching resistor. Two types of single-channel resistive-anode prototype were produced at the CERN EP-DT-DD Micro-Pattern Technologies (MPT) workshop, featuring active areas of  $\varnothing 10 \text{ mm}$  and  $\varnothing 15 \text{ mm}$ . To estimate the fundamental signal attenuation factor in Eq. 14, information on the insulating layer and the amplification gap thickness is required. Although metal and resistive anode detectors are nominally manufactured with identical bottom insulating layer thicknesses, small variations can arise from production tolerances. Therefore, a measurement of the distance between the anode surface and the top of the calendared micro-mesh was performed using a Hirox RH-2000 digital microscope [56] by focusing on surface imperfections on both electrodes through the mechanical movement of the apparatus. The measured amplification gap sizes are  $(134.9 \pm 1.4) \mu\text{m}$  and  $(139.4 \pm 1.4) \mu\text{m}$  for the metallic and resistive-anode detectors, respectively.

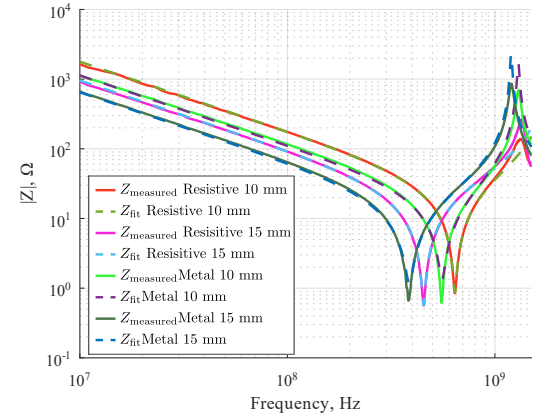


Figure 9: Measured impedance of metal and resistive anode detectors with  $10 \text{ mm}$  and  $15 \text{ mm}$  diameter pad areas, with the fit overlaid as dash lines.

## 4. Experimental verification

### 4.1. Measurements of the parasitic parameters of the resistive detector

The readout pad capacitance and signal path inductance are important parameters that strongly influence the shape of the measured electron signal [19]. The impedance of both the metal and resistive-anode ( $\varnothing 10 \text{ mm}$  and  $\varnothing 15 \text{ mm}$ ) detectors was measured over a frequency range from  $10 \text{ MHz}$  to  $1.5 \text{ GHz}$  using a Siglent SVA1032X vector network analyzer (VNA). The measurement procedure and the subsequent impedance fitting method followed the same approach as described in Ref. [19]. Fig. 9 shows the measured impedance characteristics with the corresponding fits overlaid, and a summary of all fitted parameters is provided in Table 1.

It can be observed that the measured pad capacitance of the resistive-anode detector is  $\approx 30\%$  lower than that of the metal-anode detector, while its parasitic inductance is slightly higher, possibly due to the reduced number of spring-loaded ground-connection pins. The signal connection capacitance  $C_{con}$  is significantly lower in the resistive detector as it lacks the biasing trace and biasing resistor pad, which is implemented on the Outer Board of the metal anode detector. As expected, the resistive-anode detector exhibits the reduced  $C_{pad}$  due to the addition of an insulating layer with resistive coating, but this reduction is larger than the theoretically predicted by relation Eq.

Table 1: Parameters obtained by impedance fitting.

Fit parameter	Met. anode $\varnothing 10 \text{ mm}$	Met. anode $\varnothing 15 \text{ mm}$	Res. anode $\varnothing 10 \text{ mm}$	Res. anode $\varnothing 15 \text{ mm}$
$C_{pad}, \text{pF}$	$11.49 \pm 0.27$	$22.02 \pm 0.52$	$7.82 \pm 0.20$	$15.62 \pm 0.37$
$L_{\sigma}, \text{nH}$	$7.12 \pm 0.17$	$7.68 \pm 0.19$	$7.88 \pm 0.20$	$7.90 \pm 0.19$
$C_{con}, \text{pF}$	$2.59 \pm 0.73$	$2.57 \pm 0.73$	$1.04 \pm 0.11$	$1.04 \pm 0.09$
$R_s, \Omega$	$1.35 \pm 0.28$	$1.17 \pm 0.26$	$0.87 \pm 0.30$	$0.57 \pm 0.21$

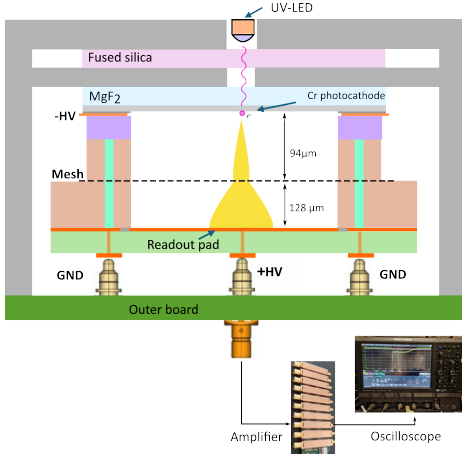


Figure 10: Schematic representation of the experimental setup used for the single-photoelectron signal dynamics measurements. The PICOSEC MM detector is operated with a semi-transparent Cr photocathode on an  $\text{MgF}_2$  radiator and illuminated by a pulsed UV LED. The induced signal on the readout pad is amplified by a custom preamplifier and digitized by a fast oscilloscope.

(A.3). This discrepancy may arise from the contribution of the parasitic capacitance, such as those introduced by the  $200\ \mu\text{m}$  bottom insulator covering the readout pad of the metal-anode detector, the capacitance between the readout pad and the surrounding ground ring, and the capacitance between the readout pad spring-loaded pin and the ground pins.

#### 4.2. Signal dynamics measurements

To investigate the impact of an insulating layer with a resistive DLC coating added on top of the readout pad on the detector performance, measurements of the output signal dynamics were carried out for detectors with metal and resistive anodes using single photoelectron under laboratory conditions. Measurements were performed on  $\varnothing 10\ \text{mm}$  active area metal or resistive anode detectors with a semi-transparent Cr photocathode. The amplification and drift gap thicknesses were  $128\ \mu\text{m}$  and  $94\ \mu\text{m}$ , respectively. The induced signal from the readout pad is amplified with a custom-made low-noise preamplifier and digitized at a sampling rate of  $10\ \text{GS/s}$  by a LeCroy WR8104 oscilloscope, as shown in Fig. 10 [57, 58].

##### 4.2.1. Waveform and PSD analysis for different field configuration

Multiple runs were recorded at different anode or cathode voltages to analyze the shape of the signal. To obtain representative waveforms and reduce the noise in the ion tail region, the signals of the detector were averaged in both the frequency and time domain for the same selected e-peak amplitude range. In this way, it was possible to compare signal characteristics under different field settings.

Fig. 11 and 12 show the waveforms (top) and power spectral densities (bottom) obtained by averaging approx. 1000 waveforms or spectra of individual events recorded at a fixed anode voltage and three different cathode voltages for the metallic and

resistive detectors. Signals with an e-peak amplitude between  $55\ \text{mV}$  and  $60\ \text{mV}$  were selected for analysis. It can be observed that the signal shape remains unchanged for different cathode voltage settings in both detector types, indicating that the signal shape is independent of the cathode voltage, i.e., the drift field strength.

The same analysis was performed for a fixed cathode voltage and three different anode voltages for both the metallic and resistive detectors. In the top and bottom Fig. 13 and 14, it can be observed that only the shape of the ion tail is affected by the change of anode voltage, i.e., the amplification field, while the shape of the e-peak leading edge remains unchanged. This indicates that the dynamics of the measured e-peak signal are dominated by parasitic elements and the amplifier's bandwidth, suggesting that the actual induced signal on the anode is significantly faster.

##### 4.2.2. Comparison of the detectors

Measurements for detectors with metal and resistive-anodes were performed at the same amplification in order to enable a direct comparison. Owing to small geometrical differences between the two detectors, the detector biasing were adjusted accordingly to achieve the same effective gain. As in Sec. 2.1.2, the gain measurements were performed using a floating picoammeter [59] connected to the anode bias line. The readout electrode was connected to a charge preamplifier (ORTEC 142 IH) and a shaper (ORTEC 474), and finally to a digital MCA that recorded the event rate and amplitude spectrum, as shown in Fig. 15.

Fig. 16 (top) shows the recorded amplitude spectrum of the metal and resistive-anode detectors operated at the same effective gain. It can be observed that the metallic detector has a higher mean amplitude value than the resistive-anode detector. This behavior is expected due to the fundamental signal reduction factor, Eq. (14), that influences the induction of the signal over the dielectric. The spectrum for both the metal and resistive detectors becomes comparable when the spectrum of the former is scaled by the theoretical attenuation factor of 0.89, as shown in Fig. 16 (bottom).

Signal characteristics of both detectors measured with the same custom made preamplifier were compared at identical detector amplification obtained by the previously described procedure. Events with the same maximum electron-peak amplitude values within the ranges  $20 - 25\ \text{mV}$ ,  $40 - 45\ \text{mV}$ ,  $60 - 65\ \text{mV}$ ,  $85 - 90\ \text{mV}$ ,  $100 - 105\ \text{mV}$ ,  $120 - 125\ \text{mV}$ , and  $140 - 145\ \text{mV}$  were selected for analysis. Fig. 17 shows averaged waveforms for the metal and resistive-anode detectors for events with amplitude values between  $140\ \text{mV}$  and  $145\ \text{mV}$ . The top and bottom subfigures display zoomed-in views of the electron peak and ion tail regions, respectively, for averaged waveforms corresponding to all maximum electron-peak amplitude ranges from  $20$  to  $140\ \text{mV}$ .

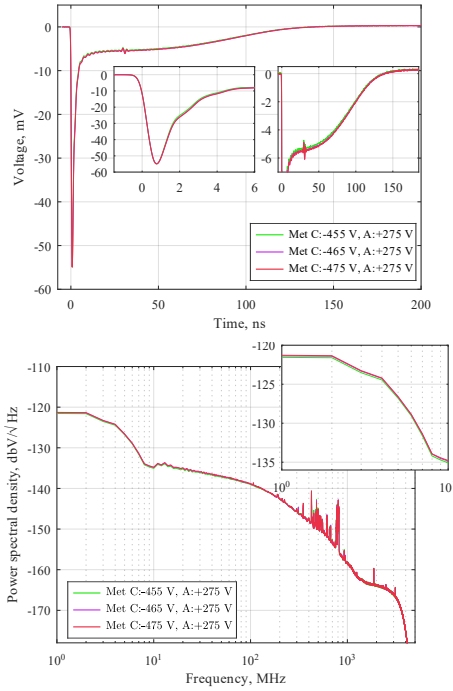


Figure 11: Averaged waveforms (top) and power spectral density (bottom) for measurements with a metal detector at a fixed anode voltage of 275 V and cathode voltages of -455 V, -465 V, and -475 V.

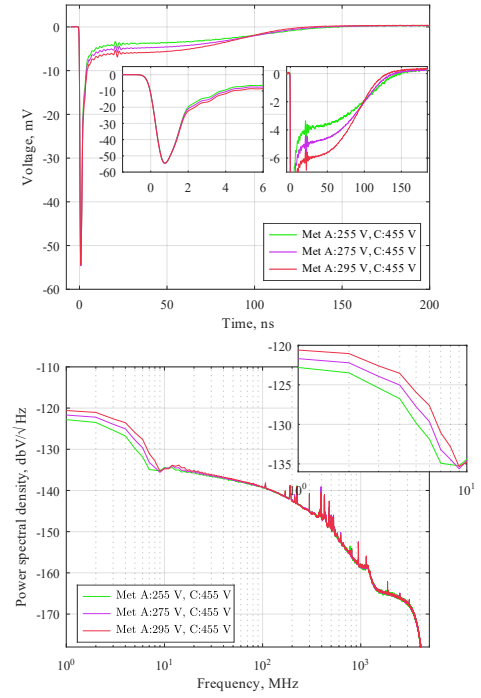


Figure 13: Averaged waveforms (top) and power spectral density (bottom) for measurements with a metal detector at a fixed cathode voltage of -455 V and anode voltages of 255 V, 275 V, and 295 V.

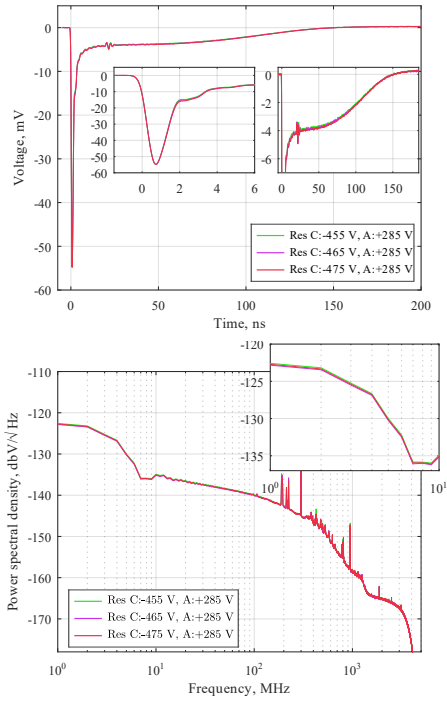


Figure 12: Averaged waveforms (top) and power spectral density (bottom) for measurements with a resistive detector at a fixed anode voltage of 285 V and cathode voltages of -455 V, -465 V, and -475 V.

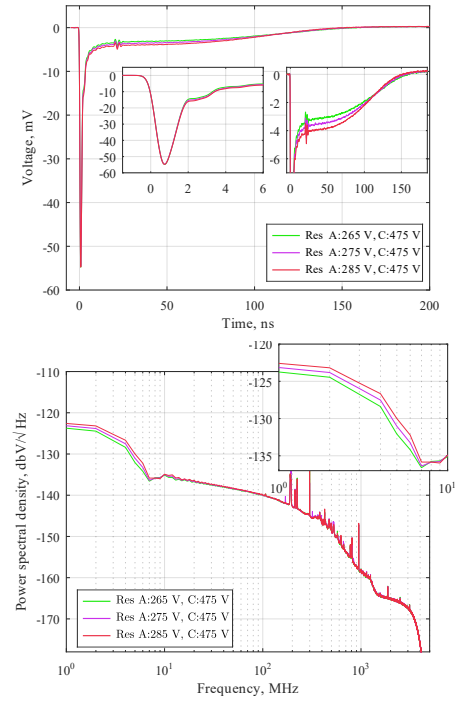


Figure 14: Averaged 1000 waveforms (top) and power spectral density (bottom) for measurements with a resistive detector at a fixed cathode voltage of -475 V and anode voltages of 265 V, 275 V, and 285 V.

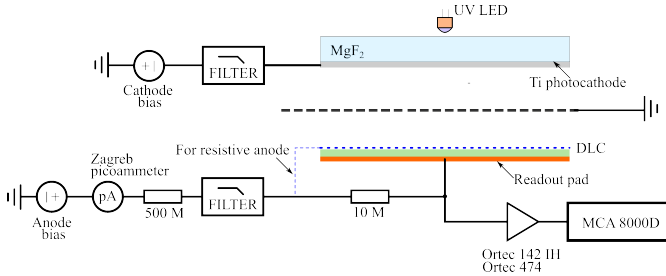


Figure 15: Schematic of PICOSEC MM detector cross section and powering circuit.

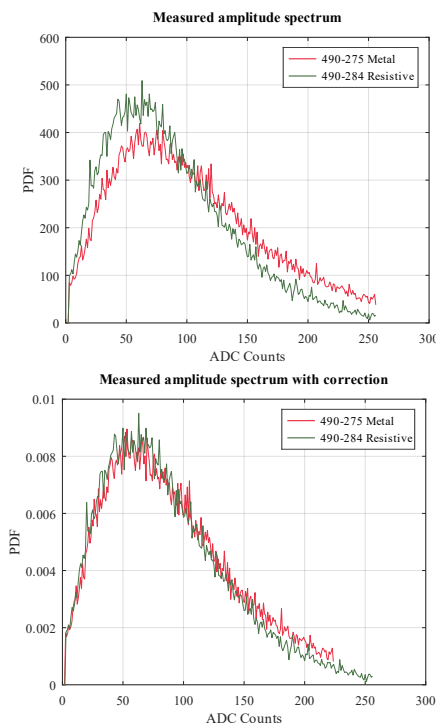


Figure 16: Top: Amplitude spectrum of metal and resistive anode detectors measured at the same gain. Bottom: Comparison of the resistive anode detector amplitude spectrum with the metal anode detector spectrum scaled by a signal reduction factor of 0.89.

The shape of the electron-peak leading edge is almost identical for all amplitudes, although the the averaged waveform with electron-peak amplitude value between 140 mV and 145 mV show slightly steeper rising edge for the resistive-anode detector. In contrast, the falling edge of the electron peak is broader for the metal-anode detector at all measured amplitudes, which may be partially attributed to its larger capacitance. Moreover, the ion tail exhibits a larger amplitude and a shorter duration in the metal-anode detector compared to the resistive-anode detector.

These similarities and differences in signal shape are shown more clearly in Fig. 18, where all averaged waveforms are normalized to the electron-peak amplitude. The observed differences in the ion tail shape may between metal and resistive de-

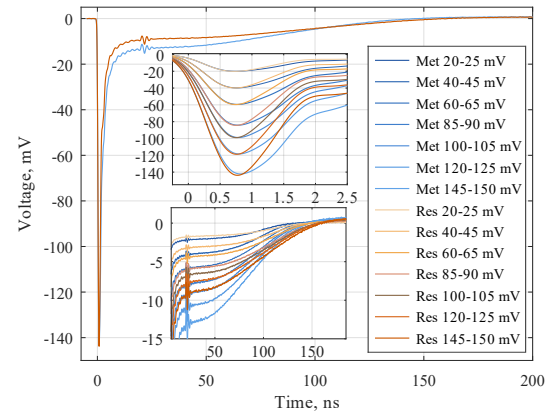


Figure 17: Averaged waveforms of metal (blue color) and resistive (orange color) anode detectors with the same electron peak amplitude value between 140 mV and 145 mV. Top sub-figure: the electron peak regions of averaged waveforms with maximum electron peak amplitude value between 20-25, 40-45, 60-65, 85-90, 100-105, 120-125, and 140-145 mV. Bottom sub-figure: Zoomed in ion tail part of the signal corresponding to the e-peak part of the signals.

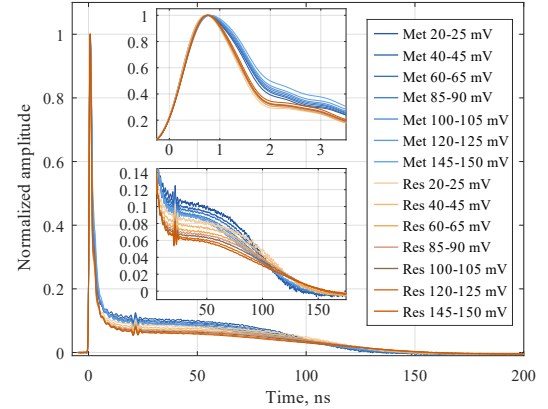


Figure 18: Normalized averaged waveforms with the respect to the maximum e-peak amplitude of metal (blue color) and resistive (orange color) anode detectors with the same electron peak amplitude value between 20 mV and 25 mV, 40 mV and 45 mV, 60 mV and 65 mV, 85 mV and 90 mV, 100 mV and 105 mV, 120 mV and 125 mV, and 140 mV and 145 mV. Top sub-figure: Zoomed in electron peak part of the signals. Bottom sub-figure: Zoomed in ion tail part of the signals.

tector, in part, be attributed to the delayed component of the induced signal associated with the resistive layer. Furthermore, Fig 18 shows that the normalized ion tail plateau reduces with the signal amplitude. This behavior is observed for both metal and resistive detector. This observed non-linearity could be attributed to the space-charge effect during the drift of the ions; however, this needs to be further investigated. Nevertheless, it is important to note that the electron-peak leading-edge characteristics remain unchanged with the addition of the resistive layer, suggesting that the timing performance of the resistive-anode detector is expected to be comparable to, or better than, that of its metallic counterpart.

#### 4.3. Detector time response with muon test beam

The time response for both types of the single-channel detectors was measured using 150 GeV muons at CERN at the SPS secondary beamline H4. An identical experimental setup to that described in Ref. [19] was used, consisting of a tracker telescope composed of three triple-GEM detectors and a timing reference and trigger detector based on an MCP-PMT<sup>7</sup>. The timing performance of  $\varnothing 10$  mm PICOSEC Micromegas detectors with metal and resistive-anodes was evaluated using either CsI or DLC photocathodes. The CsI photocathode, with a thickness of 3 nm, was deposited on a 2.38 nm Ti conductive layer on an  $\text{MgF}_2$  substrate, while the 1.5 nm thick DLC photocathode [32] was deposited directly on  $\text{MgF}_2$ . It was observed that stable operation required a larger drift-gap thickness for the CsI photocathode than for the DLC configuration, namely 120  $\mu\text{m}$  and 94  $\mu\text{m}$ , respectively.

The PICOSEC Micromegas readout chain consisted of the custom-made preamplifiers and an oscilloscope for signal amplification and digitization. The same oscilloscope was also used to record the serial bitstream containing the event ID information from the tracker, as well as the signal from the timing reference detector (MCP-PMT), which was split twice prior to being connected to the oscilloscope. The oscilloscope was operated with an analog bandwidth of 1 GHz, a sampling rate of 10 GS/s, and a vertical scale of 50 mV/div or 100 mV/div for measurements performed with DLC and CsI photocathodes, respectively.

The detector timing performance was analyzed using the same methods as described in Refs. [13, 60]. The timing marks for the PICOSEC Micromegas detector and MCP-PMT were obtained at the 20% constant fraction (CF) from a generalized logistic function fit to the leading edge of the signals. The time resolution was then determined from the distribution of the time differences between the PICOSEC MM and MCP-PMT time marks. Prior to the calculation of the time resolution, several selection criteria were applied to the triggered events in order to define the time-difference distribution:

- A time window cut of  $\pm 300$  ps around the median time difference was applied to reject outliers.
- Additional cuts were imposed on the minimum and maximum signal amplitudes.
- Geometrical cuts were applied to the reconstructed event position, retaining only events within a specified diameter around the pad center.
- Since the projection of the Cherenkov light cone onto the photocathode surface has a diameter of approximately 6 mm, a tight cut of 4 mm around the pad center was applied to ensure that all contributing photoelectrons were included.

<sup>7</sup>Hamamatsu Microchannel plate photomultiplier tube (MCP-PMT) R3809U-50 <https://www.hamamatsu.com/jp/en/product/type/R3809U-50/index.html>

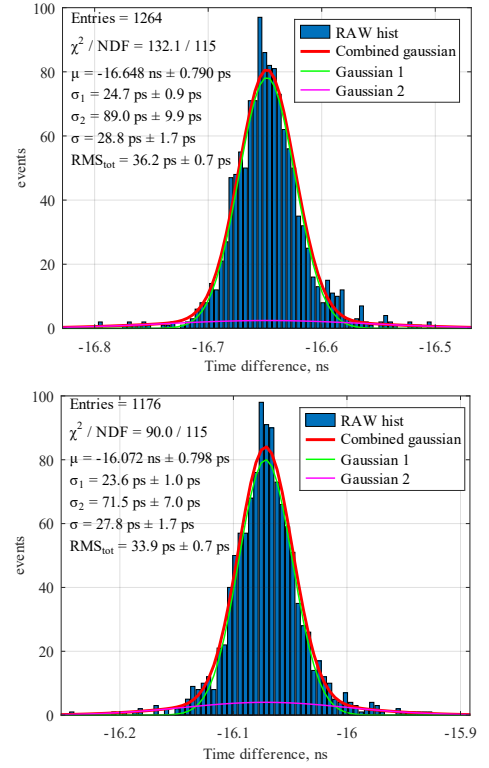


Figure 19: Time difference distribution for 150 GeV muons passing within  $\varnothing 4$  mm pad center. Top: Metal anode detector ( $\varnothing 10$  mm) with 1.5 nm thick DLC photocathode at cathode and anode voltages of -465 V and 275 V, respectively. Bottom: Resistive anode detector ( $\varnothing 10$  mm) with 1.5 nm thick DLC photocathode at cathode and anode voltages of -465 V and 285 V, respectively.

- To evaluate the timing performance over nearly the full active area, a wider geometrical cut of 9 mm around the pad center was also applied.

The detector time resolution was extracted as the standard deviation of a fit to the time-difference distribution using the sum of two Gaussian functions with a common mean value, following the procedure described in Ref. [13].

Fig. 19 (top and bottom) shows the time-difference distributions for 150 GeV muons traversing the central 4 mm-diameter region of the metal and resistive-anode detectors, respectively. An amplitude cut was applied to the PICOSEC MM signals, selecting events with amplitudes between 4 mV and 396 mV. Both detectors were equipped with a 1.5 nm DLC photocathode and a 94  $\mu\text{m}$  drift gap. The cathode voltage was set to -465 V for both detectors, while the anode voltages were adjusted to 275 V for the metal-anode detector and 285 V for the resistive-anode detector in order to operate at identical effective gain. As a result, the metal and resistive-anode detectors achieved time resolutions of  $28.8 \pm 1.7$  ps and  $27.8 \pm 0.7$  ps, respectively. When the geometrical cut was expanded to include events over nearly the entire active area ( $\varnothing 9$  mm), the time resolution degraded slightly to  $32.7 \pm 0.8$  ps and  $31.0 \pm 0.9$  ps for the metal and resistive-anode detectors, respectively. The modest degradation observed for the wider geometrical cut is expected,

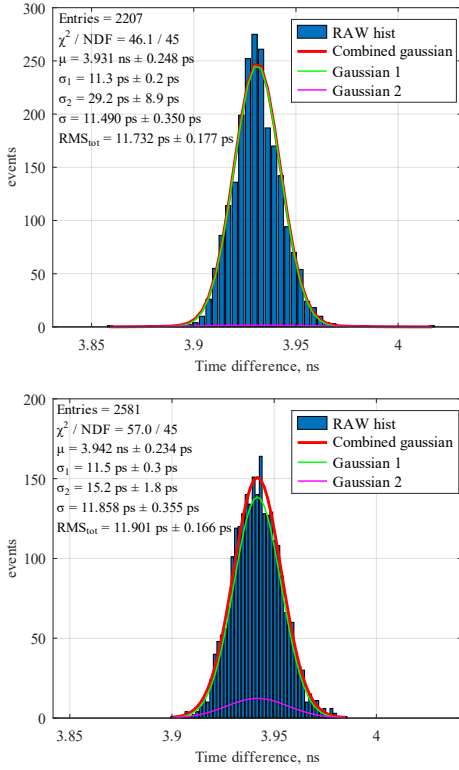


Figure 20: Time difference distribution for 150 GeV muons passing within  $\varnothing 4$  mm pad center for detectors with CsI photocathode. Top: Metal anode detector ( $\varnothing 10$  mm) operated at cathode and anode voltages of -435 V and 275 V, respectively. Bottom: Resistive anode detector ( $\varnothing 10$  mm) operated at cathode and anode voltages of -435 V and 284 V, respectively.

as a fraction of the photoelectrons is produced outside the effective active area of the detector. Nevertheless, in both cases, the two detectors exhibit very similar timing performance.

In addition to the measurements using a DLC photocathode, the performance of both detectors was also evaluated using a 3 nm thick CsI photocathode with higher quantum efficiency. For these measurements, both detectors were operated with identical drift-gap thicknesses of 120  $\mu\text{m}$  and at the same cathode voltage of -435 V. As before, to achieve identical effective gain, the anode voltages were set to 275 V for the metal-anode detector and 284 V for the resistive-anode detector. Fig. 20 shows the time-difference distributions for 150 GeV muons traversing the central 4 mm-diameter region of the metal (top) and resistive-anode (bottom) detectors. The metal-anode detector achieves a time resolution of  $11.5 \pm 0.4$  ps, while the resistive-anode detector exhibits a resolution of  $11.9 \pm 0.4$  ps, with no statistically significant difference observed between the two. This close agreement indicates that, although the addition of a resistive coating on the insulating layer above the readout pad introduces an inherent reduction in signal induction, the detector maintains excellent timing performance. When the geometrical cut was expanded to include events within a  $\varnothing 9$  mm region around the pad center, time resolutions of  $13.1 \pm 0.2$  ps and  $13.4 \pm 0.5$  ps were obtained for the metal and resistive-anode

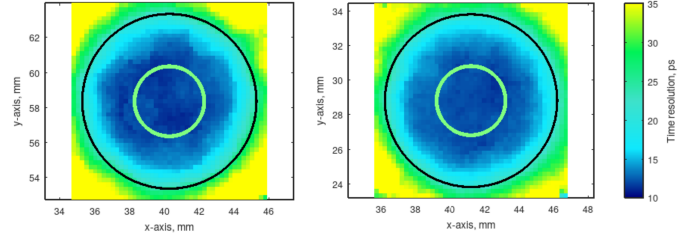


Figure 21: Time resolution over the pad area for metal (left) and resistive (right) anode detectors. The black circle indicates the pad's active area ( $\varnothing 10$  mm), while the green circle at the centre marks  $\varnothing 4$  mm region where the Cherenkov cone from particles passing through this area is fully contained within the pad.

detectors, respectively. This suggests that, despite the partial loss of photoelectrons outside the active area, the number of detected photoelectrons remains sufficient to sustain high signal amplitudes and good timing resolution, close to that measured at the pad center. This behavior is also illustrated by the two-dimensional maps of the time resolution across the full detector area shown in Fig. 21 (left and right), where both detector types exhibit uniform and mutually consistent performance over the entire active surface.

## 5. Conclusion

A resistive-anode implementation of the PICOSEC Micromegas detector was developed and characterized with the aim of improving robustness against discharges and enabling future multi-channel operation while preserving excellent timing performance. A comprehensive study combining analytical modeling, finite-element simulations, and experimental measurements was performed to assess the impact of the resistive layer on rate capability, signal formation, and time resolution.

The rate capability of the resistive readout structure was investigated through analytical calculations and FEM simulations of the voltage drop induced by intense irradiation on a finite-size resistive layer. For the single-channel geometry and expected beam conditions at the CERN SPS H4 beam line, surface resistivities around  $20 \text{ M}\Omega/\square$  were found to provide an optimal compromise between discharge protection and gain stability. In addition, the influence of the resistive layer on signal integrity was studied using an extended Ramo-Shockley formalism with time-dependent weighting fields and Garfield++ simulations. The contribution of delayed signal components due to the finite conductivity of the DLC layer was quantified, and it was shown that for surface resistivities exceeding approximately  $100 \text{ k}\Omega/\square$ , the leading edge of the electron peak remains unaffected. While the presence of the insulating layer introduces a fundamental reduction in signal amplitude of about 11%, laboratory measurements with single photoelectrons confirmed that the electron-peak dynamics and leading-edge characteristics are preserved for the chosen

resistivity range.

Two resistive-anode prototype detectors with active areas of  $\varnothing 10$  mm and  $\varnothing 15$  mm were designed, constructed, and experimentally characterized. Measurements of parasitic capacitances and inductances confirmed the expected changes induced by the resistive layout, which were found to be compatible with fast signal readout. Direct comparisons between metallic and resistive-anode detectors demonstrated consistent signal shapes of the electron-peak under comparable operating conditions, while a difference in both the width of the electron-peak and ion tails were observed. In addition, using a charge sensitive, the 11% signal attenuation predicted from signal modeling was observed. Finally, beam tests with 150 GeV muons at CERN using both DLC and CsI photocathodes demonstrated that the resistive-anode detector achieves a time resolution fully comparable to that of the metallic-anode configuration. With a CsI photocathode, a resolution of  $11.9 \pm 0.4$  ps was measured for the resistive detector, in agreement within uncertainties with the  $11.5 \pm 0.4$  ps obtained for the metallic reference. The timing performance was found to be uniform across the active area, confirming that the resistive layer does not degrade the intrinsic time resolution. These results demonstrate that a resistive-anode PICOSEC Micromegas detector can maintain excellent timing performance while providing enhanced operational robustness.

## Appendix A. Signal amplitude and detector capacitance

The signal attenuation caused by the presence of the insulating laminate in the resistive layout can be estimated from the ratio of the detector capacitances of the metal-anode and resistive-anode detectors. For a metallic anode, the capacitance is given by

$$C_{\text{met}} = \varepsilon_0 \frac{A}{g}, \quad (\text{A.1})$$

while for the resistive configuration it becomes

$$C_{\text{res}} = \varepsilon_0 \varepsilon_r \frac{A}{\varepsilon_r g + d}. \quad (\text{A.2})$$

Here  $A$  denotes the readout-pad area,  $g$  the amplification gap size,  $\varepsilon_0$  the permittivity of free space, and  $\varepsilon_r$  and  $d$  the relative permittivity and thickness of the insulating layer, respectively. Taking the ratio yields

$$\frac{C_{\text{res}}}{C_{\text{met}}} = 1 - \frac{d}{d + \varepsilon_r g}, \quad (\text{A.3})$$

which corresponds to the signal reduction factor defined in Eq. 14. As a result, this factor may be determined empirically by measuring the capacitances, provided that parasitic contributions are negligible.

## Acknowledgements

We thank the CERN-EP-DT-MPT Workshop, particularly Antonio Teixeira, Olivier Pizzirusso, Bertrand Mehl and Rui

de Oliveira for the useful discussion and production of MM prototypes with resistive anode. We acknowledge the financial support of the EP R&D, CERN Strategic Programme on Technologies for Future Experiments; the RD51 Collaboration, in the framework of RD51 common projects; the Cross-Disciplinary Program on Instrumentation and Detection of CEA, the French Alternative Energies and Atomic Energy Commission; the PHENIICS Doctoral School Program of Université Paris-Saclay, France; the Program of National Natural Science Foundation of China (grant number 11935014, 12125505); the COFUND-FP-CERN-2014 program (grant number 665779); the Fundação para a Ciência e a Tecnologia (FCT), Portugal; the Enhanced Eurotalents program (PCOFUND-GA-2013-600382); the US CMS program under DOE contract No. DE-AC02-07CH11359. This material is based upon work supported by the U.S. Department of Energy, Office of Science, Office of Nuclear Physics under contracts DE-AC05-06OR23177. The project is funded by the European Union under the NextGenerationEU Programme.

## References

- [1] ECFA Detector R&D Roadmap Process Group, [The 2021 ECFA detector research and development roadmap](#), Tech. rep., CERN, Geneva (2020). URL <https://cds.cern.ch/record/2784893>
- [2] A. Cardini, G. Bencivenni, P. De Simone, The operational experience of the triple-gem detectors of the lhcb muon system: Summary of 2 years of data taking, in: 2012 IEEE Nuclear Science Symposium and Medical Imaging Conference Record (NSS/MIC), 2012, pp. 759–762. [doi:10.1109/NSSMIC.2012.6551204](https://doi.org/10.1109/NSSMIC.2012.6551204).
- [3] M. Poli-Lener, Triple-gem detectors for the innermost region of the muon apparatus at the lhcb experiment (May 2005).
- [4] B. Ketzer, Q. Weitzel, S. Paul, F. Sauli, L. Ropelewski, Performance of triple gem tracking detectors in the compass experiment, Nuclear Instruments and Methods in Physics Research Section A: Accelerators, Spectrometers, Detectors and Associated Equipment 535 (1) (2004) 314–318, proceedings of the 10th International Vienna Conference on Instrumentation. [doi:https://doi.org/10.1016/j.nima.2004.07.146](https://doi.org/10.1016/j.nima.2004.07.146).
- [5] M. Ziegler, Development of a triple GEM detector for the LHCb experiment, [Dissertation](#), University of Zurich (2002).
- [6] D. Abbaneo, C. Armagnaud, M. Abbrescia, P. Aspell, S. Bally, et al., Gem based detector for future upgrade of the cms forward muon system, Nuclear Instruments and Methods in Physics Research Section A: Accelerators, Spectrometers, Detectors and Associated Equipment 718 (2013) 383–386, proceedings of the 12th Pisa Meeting on Advanced Detectors. [doi:https://doi.org/10.1016/j.nima.2012.10.058](https://doi.org/10.1016/j.nima.2012.10.058).
- [7] T. Kawamoto, S. Vlachos, L. Pontecorvo, J. Dubbert, G. Mikenberg, P. Iengo, C. Dallapiccola, C. Amelung, L. Levinson, R. Richter, D. Lelouch, [New Small Wheel Technical Design Report](#), Tech. rep., CERN, Geneva, aTLAS New Small Wheel Technical Design Report (2013). URL <https://cds.cern.ch/record/1552862>
- [8] The ALICE Collaboration, [Upgrade of the ALICE Time Projection Chamber](#), Tech. rep., CERN, Geneva (2013). URL <https://cds.cern.ch/record/1622286>
- [9] G. Charpak, P. Fonte, V. Peskov, F. Sauli, D. Scigocki, D. Stuart, Investigation of operation of a parallel-plate avalanche chamber with a csi photocathode under high gain conditions, Nuclear Instruments and Methods in Physics Research Section A: Accelerators, Spectrometers, Detectors and Associated Equipment 307 (1) (1991) 63–68. [doi:https://doi.org/10.1016/0168-9002\(91\)90131-9](https://doi.org/10.1016/0168-9002(91)90131-9).
- [10] J. Derré, Y. Giomataris, P. Reboursard, H. Zaccione, J. Perroud, G. Charpak, Fast signals and single electron detection with a micromegas photodetector, Nuclear Instruments and Methods in Physics Research Section A: Accelerators, Spectrometers, Detectors and Associated Equipment 535 (1) (2004) 319–322. [doi:https://doi.org/10.1016/j.nima.2004.07.147](https://doi.org/10.1016/j.nima.2004.07.147).

ment 449 (1) (2000) 314–321. [doi:\[https://doi.org/10.1016/S0168-9002\\(99\\)01452-7\]\(https://doi.org/10.1016/S0168-9002\(99\)01452-7\)](https://doi.org/10.1016/S0168-9002(99)01452-7).

[11] A. Breskin, A. Buzulutskov, R. Chechik, Gem photomultiplier operation in cf4, Nuclear Instruments and Methods in Physics Research Section A: Accelerators, Spectrometers, Detectors and Associated Equipment 483 (3) (2002) 670–675. [doi:\[https://doi.org/10.1016/S0168-9002\\(01\\)01940-4\]\(https://doi.org/10.1016/S0168-9002\(01\)01940-4\)](https://doi.org/10.1016/S0168-9002(01)01940-4).

[12] Y. Giomataris, P. Rebougeard, J. P. Robert, G. Charpak, MICROMEGAS: a high-granularity position-sensitive gaseous detector for high particle-flux environments, Nuclear Instruments and Methods in Physics Research Section A: Accelerators, Spectrometers, Detectors and Associated Equipment 376 (1) (1996) 29–35. [doi:\[https://doi.org/10.1016/0168-9002\\(96\\)00175-1\]\(https://doi.org/10.1016/0168-9002\(96\)00175-1\)](https://doi.org/10.1016/0168-9002(96)00175-1).

[13] J. Bortfeldt, F. Brunbauer, C. David, D. Desforge, et al., PICOSEC: Charged particle timing at sub-25 picosecond precision with a Micromegas based detector, Nuclear Instruments and Methods in Physics Research Section A: Accelerators, Spectrometers, Detectors and Associated Equipment 903 (2018) 317–325. [doi:<https://doi.org/10.1016/j.nima.2018.04.033>](https://doi.org/10.1016/j.nima.2018.04.033).

[14] L. Sohl, Development of picosec-micromegas for fast timing in high rate environments, *PhD dissertation, Université Paris-Saclay* (2022).

[15] I. Giomataris, R. De Oliveira, S. Andriamonje, S. Aune, G. Charpak, P. Colas, G. Fanourakis, E. Ferrer, A. Giganon, P. Rebougeard, P. Salin, Micromegas in a bulk, Nuclear Instruments and Methods in Physics Research Section A: Accelerators, Spectrometers, Detectors and Associated Equipment 560 (2) (2006) 405–408. [doi:<https://doi.org/10.1016/j.nima.2005.12.222>](https://doi.org/10.1016/j.nima.2005.12.222).

[16] C. Aimè, M. Brunoldi, S. Calzaferri, D. Fiorina, C. Riccardi, P. Salvini, I. Vai, P. Vitulo, Simulation and r&d studies for the muon spectrometer at a 10tev muon collider, Nuclear Instruments and Methods in Physics Research Section A: Accelerators, Spectrometers, Detectors and Associated Equipment 1069 (2024) 169903. [doi:<https://doi.org/10.1016/j.nima.2024.169903>](https://doi.org/10.1016/j.nima.2024.169903).

[17] T. Alexopoulos, J. Burnens, R. de Oliveira, G. Glonti, O. Pizzirusso, V. Polychronakos, G. Sekhniaidze, G. Tsipolitis, J. Wotschack, A spark-resistant bulk-micromegas chamber for high-rate applications, Nuclear Instruments and Methods in Physics Research Section A: Accelerators, Spectrometers, Detectors and Associated Equipment 640 (1) (2011) 110–118. [doi:<https://doi.org/10.1016/j.nima.2011.03.025>](https://doi.org/10.1016/j.nima.2011.03.025).

[18] G. Bencivenni, R. D. Oliveira, G. Morello, M. P. Lener, The micro-Resistive WELL detector: a compact spark-protected single amplification-stage MPGD, Journal of Instrumentation 10 (02) (2015) P02008. [doi:\[10.1088/1748-0221/10/02/P02008\]\(https://doi.org/10.1088/1748-0221/10/02/P02008\)](https://doi.org/10.1088/1748-0221/10/02/P02008).

[19] A. Utrobicic, R. Aleksan, Y. Angelis, J. Bortfeldt, F. Brunbauer, M. Brunoldi, E. Chatzianagnostou, J. Datta, K. Dehmelt, G. Fanourakis, et al., Single channel picosec micromegas detector with improved time resolution, Nuclear Instruments and Methods in Physics Research Section A: Accelerators, Spectrometers, Detectors and Associated Equipment 1072 (2025) 170127. [doi:<https://doi.org/10.1016/j.nima.2024.170127>](https://doi.org/10.1016/j.nima.2024.170127).

[20] A. Einstein, Zur theorie der brownschen bewegung, Annalen der Physik 324 (2) (1906) 371–381. [doi:<https://doi.org/10.1002/andp.19063240208>](https://doi.org/10.1002/andp.19063240208).

[21] J. B. Johnson, Thermal agitation of electricity in conductors, Physical Review 32 (1928) 97. [doi:\[10.1103/PhysRev.32.97\]\(https://doi.org/10.1103/PhysRev.32.97\)](https://doi.org/10.1103/PhysRev.32.97).

[22] H. Nyquist, Thermal agitation of electric charge in conductors, Physical Review 32 (1928) 110. [doi:\[10.1103/PhysRev.32.110\]\(https://doi.org/10.1103/PhysRev.32.110\)](https://doi.org/10.1103/PhysRev.32.110).

[23] D. Janssens, W. Riegler, Noise in detectors containing distributed resistive elements, Nuclear Instruments and Methods in Physics Research Section A: Accelerators, Spectrometers, Detectors and Associated Equipment 1064 (2024) 169374. [doi:<https://doi.org/10.1016/j.nima.2024.169374>](https://doi.org/10.1016/j.nima.2024.169374).

[24] J. Galán, D. Attié, A. Chaus, P. Colas, A. Delbart, E. Ferrer-Ribas, I. Giomataris, F. Iguaz, A. Gongadze, T. Papaevangelou, A. Peyaud, Characterization and simulation of resistive-mpgds with resistive strip and layer topologies, Nuclear Instruments and Methods in Physics Research Section A: Accelerators, Spectrometers, Detectors and Associated Equipment 732 (2013) 229–232, vienna Conference on Instrumentation 2013. [doi:<https://doi.org/10.1016/j.nima.2013.08.011>](https://doi.org/10.1016/j.nima.2013.08.011).

[25] M. S. Dixit, J. Dubeau, J. P. Martin, K. Sachs, Position sensing from charge dispersion in micro-pattern gas detectors with a resistive anode, Nuclear Instruments and Methods in Physics Research, Section A: Accelerators, Spectrometers, Detectors and Associated Equipment 518 (2004) 721–727. [doi:\[10.1016/j.nima.2003.09.051\]\(https://doi.org/10.1016/j.nima.2003.09.051\)](https://doi.org/10.1016/j.nima.2003.09.051).

[26] Z. Fang, S. He, H. Zhou, Y. Lv, Y. Zhou, J. Liu, M. Shao, Z. Zhang, Simulation and optimization of fast grounding designs for micro-pattern gas detectors with a resistive layer, Nuclear Instruments and Methods in Physics Research Section A: Accelerators, Spectrometers, Detectors and Associated Equipment 1032 (2022) 166615. [doi:<https://doi.org/10.1016/j.nima.2022.166615>](https://doi.org/10.1016/j.nima.2022.166615).

[27] G. Bencivenni, R. de Oliveira, G. Felici, M. Gatta, M. Giovannetti, G. Morello, A. Ochi, M. P. Lener, E. Tskhadadze, The  $\mu$ -RWELL layouts for high particle rate, Journal of Instrumentation 14 (05) (2019) P05014. [doi:\[10.1088/1748-0221/14/05/P05014\]\(https://doi.org/10.1088/1748-0221/14/05/P05014\)](https://doi.org/10.1088/1748-0221/14/05/P05014).

[28] M. Chefdeville, Y. Karyotakis, T. Geralis, M. Titov, Resistive micromegas for sampling calorimetry, a study of charge-up effects, Nuclear Instruments and Methods in Physics Research Section A: Accelerators, Spectrometers, Detectors and Associated Equipment 824 (2016) 510–511, frontier Detectors for Frontier Physics: Proceedings of the 13th Pisa Meeting on Advanced Detectors. [doi:<https://doi.org/10.1016/j.nima.2015.11.073>](https://doi.org/10.1016/j.nima.2015.11.073).

[29] M. Alviggi, M. Biglietti, V. Canale, M. D. Pietra, C. D. Donato, S. Franchino, P. Iengo, M. Iodice, F. Petrucci, G. Sekhniaidze, O. Sidiropoulou, Small-pads resistive micromegas, Journal of Instrumentation 12 (03) (2017) C03077. [doi:\[10.1088/1748-0221/12/03/C03077\]\(https://doi.org/10.1088/1748-0221/12/03/C03077\)](https://doi.org/10.1088/1748-0221/12/03/C03077).

[30] M. Iodice, et al., Small-pad resistive micromegas: Comparison of patterned embedded resistors and dlc based spark protection systems., Journal of Physics: Conference Series 1498 (2020) 012028. [doi:\[10.1088/1742-6596/1498/1/012028\]\(https://doi.org/10.1088/1742-6596/1498/1/012028\)](https://doi.org/10.1088/1742-6596/1498/1/012028).

[31] M. Iodice, M. Alviggi, M. Camerlingo, V. Canale, M. D. Pietra, C. D. Donato, P. Iengo, F. Petrucci, E. Rossi, G. Sekhniaidze, Small-pad resistive micromegas: rate capability for different spark protection resistive schemes, Journal of Instrumentation 15 (09) (2020) C09043. [doi:\[10.1088/1748-0221/15/09/C09043\]\(https://doi.org/10.1088/1748-0221/15/09/C09043\)](https://doi.org/10.1088/1748-0221/15/09/C09043).

[32] M. Lisowska, R. Aleksan, Y. Angelis, S. Aune, J. Bortfeldt, F. Brunbauer, M. Brunoldi, E. Chatzianagnostou, J. Datta, K. Dehmelt, et al., Photocathode characterisation for robust picosec micromegas precise-timing detectors, Nuclear Instruments and Methods in Physics Research Section A: Accelerators, Spectrometers, Detectors and Associated Equipment 1072 (2025) 170151. [doi:<https://doi.org/10.1016/j.nima.2024.170151>](https://doi.org/10.1016/j.nima.2024.170151).

[33] W. Riegler, Electric fields, weighting fields, signals and charge diffusion in detectors including resistive materials, Journal of Instrumentation 11 (11) (feb 2016). [arXiv:1602.07949v1](https://arxiv.org/abs/1602.07949v1), [doi:\[10.1088/1748-0221/11/11/P11002\]\(https://doi.org/10.1088/1748-0221/11/11/P11002\)](https://doi.org/10.1088/1748-0221/11/11/P11002).

[34] C. Lippmann, W. Riegler, A. Kalweit, Rate effects in resistive plate chambers, Nuclear Physics B - Proceedings Supplements 158 (2006) 127–130, proceedings of the 8th International Workshop on Resistive Plate Chambers and Related Detectors. [doi:<https://doi.org/10.1016/j.nuclphysbps.2006.07.037>](https://doi.org/10.1016/j.nuclphysbps.2006.07.037).

[35] J. Lehtonen, The lambert w function in ecological and evolutionary models, Methods in Ecology and Evolution 7 (9) (2016) 1110–1118. [doi:<https://doi.org/10.1111/2041-210X.12568>](https://doi.org/10.1111/2041-210X.12568).

[36] COMSOL® 6.1, Software for multiphysics simulation, <https://www.comsol.ch> (2025).

[37] D. Janssens, M. Lisowska, on behalf of the PICOSEC collaboration, Robust photocathodes and spatial resolution studies of resistive PICOSEC Micromegas precise-timing detectors, USTC, *Presented at: The 8th International Conference on Micro Pattern Gaseous Detectors*, 2024.

[38] G. Battistoni, P. Campana, V. Chiarella, U. Detti, E. Iarocci, G. Nicollotti, Resistive cathode transparency, Nuclear Instruments and Methods in Physics Research 202 (3) (1982) 459–464. [doi:\[https://doi.org/10.1016/0167-5087\\(82\\)90540-3\]\(https://doi.org/10.1016/0167-5087\(82\)90540-3\)](https://doi.org/10.1016/0167-5087(82)90540-3).

[39] W. Shockley, Currents to conductors induced by a moving point charge, Journal of Applied Physics 9 (10) (1938) 635–636. [doi:\[10.1063/1.1710367\]\(https://doi.org/10.1063/1.1710367\)](https://doi.org/10.1063/1.1710367).

[40] S. Ramo, Currents Induced by Electron Motion, Proceedings of the IRE 27 (9) (1939) 584–585. [doi:\[10.1109/JRPROC.1939.228757\]\(https://doi.org/10.1109/JRPROC.1939.228757\)](https://doi.org/10.1109/JRPROC.1939.228757).

[41] E. Gatti, G. Padovini, V. Radeka, Signal evaluation in multielectrode radiation detectors by means of a time dependent weighting vector, Nuclear Instruments and Methods in Physics Research 193 (1982) 651–653.

[doi:10.1016/0029-554X\(82\)90265-8](https://doi.org/10.1016/0029-554X(82)90265-8).

[42] W. Riegler, Induced signals in resistive plate chambers, Nuclear Instruments and Methods in Physics Research Section A: Accelerators, Spectrometers, Detectors and Associated Equipment 491 (1-2) (2002) 258-271. [doi:10.1016/S0168-9002\(02\)01169-5](https://doi.org/10.1016/S0168-9002(02)01169-5).

[43] W. Riegler, Extended theorems for signal induction in particle detectors vci 2004, Nuclear Instruments and Methods in Physics Research, Section A: Accelerators, Spectrometers, Detectors and Associated Equipment 535 (2004) 287-293. [doi:10.1016/S0168-9002\(04\)01656-0](https://doi.org/10.1016/S0168-9002(04)01656-0).

[44] W. Riegler, An application of extensions of the Ramo-Shockley theorem to signals in silicon sensors, Nuclear Instruments and Methods in Physics Research, Section A: Accelerators, Spectrometers, Detectors and Associated Equipment 940 (2019) 453-461. [arXiv:1812.07570](https://arxiv.org/abs/1812.07570), [doi:10.1016/J.NIMA.2019.06.056](https://doi.org/10.1016/J.NIMA.2019.06.056).

[45] D. Janssens, et al., Induced signals in particle detectors with resistive elements: Numerically modeling novel structures (VCI 2022), Nuclear Instruments and Methods in Physics Research Section A: Accelerators, Spectrometers, Detectors and Associated Equipment 1040 (2022) 167227. [doi:10.1016/J.NIMA.2022.167227](https://doi.org/10.1016/J.NIMA.2022.167227).

[46] D. Janssens, Resistive electrodes and particle detectors: Modelling and measurements of novel detector structures, Ph.D. thesis, Vrije Universiteit Brussel, [https://cris.vub.be/ws/portalfiles/portal/109006231/Djunes\\_Janssens\\_PhD\\_Thesis.pdf](https://cris.vub.be/ws/portalfiles/portal/109006231/Djunes_Janssens_PhD_Thesis.pdf) (2023).

[47] H. Schindler, R. Veenhof, Garfield++, <https://garfieldpp.web.cern.ch/garfieldpp> (2025).

[48] D. Janssens, Resistive electrodes and particle detectors: Modelling and measurements of novel detector structures (Mar. 2024).

[49] J. Bortfeldt, F. Brunbauer, C. David, D. Desforge, G. Fanourakis, M. Galilano, F. García, I. Giomataris, T. Gustavsson, F. Iguaz, M. Kebbiri, K. Kordas, C. Lampoudis, P. Legou, M. Lisowska, J. Liu, M. Lupberger, O. Maillard, I. Manthos, H. Müller, V. Niaouris, E. Oliveri, T. Papaeangelou, K. Paraschou, M. Pomorski, B. Qi, F. Resnati, L. Ropelewski, D. Sampsonidis, L. Scharenberg, T. Schneider, L. Sohl, M. van Stenis, Y. Tsipolitis, S. Tzamarias, A. Utrobicic, R. Veenhof, X. Wang, S. White, Z. Zhang, Y. Zhou, Modeling the timing characteristics of the picosec micromegas detector, Nuclear Instruments and Methods in Physics Research Section A: Accelerators, Spectrometers, Detectors and Associated Equipment 993 (2021) 165049. [doi:https://doi.org/10.1016/j.nima.2021.165049](https://doi.org/10.1016/j.nima.2021.165049).

[50] H. Schindler, *Microscopic simulation of particle detectors*, Technischen Universität Wien (2012).  
URL <https://cds.cern.ch/record/1500583>

[51] J. A. Hornbeck, The drift velocities of molecular and atomic ions in helium, neon, and argon, Physical Review 84 (4) (1951) 615.

[52] E. Beaty, Contribution, 5th conference on ionization phenomena in gases (1961).

[53] Y. Kalkan, M. Arslanok, A. Cortez, Y. Kaya, I. Tapan, R. Veenhof, Cluster ions in gas-based detectors, Journal of Instrumentation 10 (07) (2015) P07004. [doi:10.1088/1748-0221/10/07/P07004](https://doi.org/10.1088/1748-0221/10/07/P07004).

[54] D. J. G. Marques, A. F. V. Cortez, J. Escada, R. Veenhof, P. N. B. Neves, C. A. N. Conde, F. P. Santos, F. I. G. M. Borges, Experimental ion mobility measurements in Ne-CF<sub>4</sub>, JINST 14 (04) (2019) P04015. [doi:10.1088/1748-0221/14/04/P04015](https://doi.org/10.1088/1748-0221/14/04/P04015).

[55] Analog Devices, LTspice®, <https://www.analog.com/en/design-center/design-tools-and-calculators/ltpice-simulator.html> (2025).

[56] Hirox, Hirox rh-2000 digital microscope, Available at <https://www.hirox-europe.com/products/3d-digital-microscope/rh-2000/> (2025).

[57] C. Hoarau, G. Bosson, J.-L. Bouly, S. Curtoni, et al., RF pulse amplifier for CVD-diamond particle detectors, Journal of Instrumentation 16 (04) (2021) T04005. [doi:10.1088/1748-0221/16/04/T04005](https://doi.org/10.1088/1748-0221/16/04/T04005).

[58] M. Kovacic, Design of preamplifier cards for multipad PICOSEC detector, June 2022, PICOSEC Micromegas Collaboration meeting, [https://indico.jlab.org/event/621/contributions/11026/attachments/8892/12850/Picosec\\_amplifiers\\_MK.pdf](https://indico.jlab.org/event/621/contributions/11026/attachments/8892/12850/Picosec_amplifiers_MK.pdf).

[59] A. Utrobicic, M. Kovacic, F. Erhardt, N. Poljak, M. Planinic, A floating multi-channel picoammeter for micropattern gaseous detector current monitoring, Nuclear Instruments and Methods in Physics Research Section A: Accelerators, Spectrometers, Detectors and Associated Equipment 801 (2015) 21-26. [doi:https://doi.org/10.1016/j.nima.2015.08.021](https://doi.org/10.1016/j.nima.2015.08.021).

[60] L. Sohl, Development of PICOSEC-Micromegas for fast timing in high rate environments, Ph.D. thesis, Université Paris-Saclay, <https://theses.hal.science/tel-03167728> (2020).